Post-emplacement dynamics of andesitic lava flows at Volcán de Colima, Mexico, revealed by radar and optical remote sensing data

Alexandre Carrara, Virginie Pinel, Pascale Bascou, Emmanuel Chaljub, Servando de La Cruz-Reyna

To cite this version:

Alexandre Carrara, Virginie Pinel, Pascale Bascou, Emmanuel Chaljub, Servando de La Cruz-Reyna. Post-emplacement dynamics of andesitic lava flows at Volcán de Colima, Mexico, revealed by radar and optical remote sensing data. Journal of Volcanology and Geothermal Research, 2019, 381, pp.1 - 15. 10.1016/j.jvolgeores.2019.05.019 . hal-03480697

HAL Id: hal-03480697
https://hal.science/hal-03480697

Submitted on 20 Dec 2021

Post-emplacement dynamics of andesitic lava flows at Volcán de Colima, Mexico, revealed by radar and optical remote sensing data

Alexandre Carrara[1]*, Virginie Pinel[1], Pascale Bascou[1], Emmanuel Chaljub[1], Servando De la Cruz-Reyna[2]

[1] Univ. Grenoble Alpes, Univ. Savoie Mont Blanc, CNRS, IRD, IFSTTAR, ISTerre, 38000 Grenoble, France

[2] Instituto de Geofisica, Universidad Nacional Autónoma de Mexico, CDMX 04510, Mexico

* Corresponding author: Alexandre Carrara (carrara.alexandre.univ@gmail.com)

Highlights:-We propose a novel approach for retrieving a 3D displacement field on lava flows.

-We measure horizontal motion on a lava flow several months after its emplacement.

-Thermal contraction, loading and flow all contribute to the displacements.

Abstract : 281 words ; Main text : 9510 words, 4 tables, 11 figures, 65 references

Abstract:

We used optical and radar remote sensing datasets to map, estimate the volume, and measure the surface displacements of lava flows emplaced on the flanks of Volcán de Colima, Mexico by extrusion of lava dome material from the end of 2014 to early 2016. Our main result is that the flow motion of the lava contributes significantly to the recorded displacements several months after its emplacement. First, we mapped the deposits and estimated their volumes using two Digital Elevation Models (DEM), one derived from radar data acquired before the peak of activity and one derived from optical images acquired just after this peak of activity. Coherence information derived from the radar dataset added some temporal constraints on the timing of emplacement of various deposits. We thus estimated a mean extrusion rate of 1-2 m^3 s^{-1} between November 2014 and February 2015. We then used a new approach to reconstruct the 3D displacement field, taking advantage of images acquired by the same satellite, on both ascending and descending tracks, and using a physical *a priori* on the direction of horizontal displacements. Our results show that about 2 cm yr^{-1} of horizontal motion is still recorded a few months after the emplacement on the SW lava flow, which is the only one covered by the two-acquisition geometries. In order to differentiate the potential causes of the observed displacements, we modeled the thermal contraction of the lava flow using a finite element numerical method. Removing the contribution of thermoelastic contraction from the measured displacements enable to infer both the viscoelastic loading and flow motion effects from the residuals. Results show that, thermal contraction, flow motion and viscoelastic loading contribute significantly to the displacements recorded.

Keywords:

- Remote sensing, InSAR, 3D displacement field, lava flow, subsidence, thermal contraction.

1. Introduction:

Spaceborne remote sensing datasets, providing information with a good spatial coverage over areas that are difficult to access, have proven to be powerful tools to study lava flows. Radar images have the advantage that they are insensitive to cloud cover and solar lighting. They can be used to detect and map new lava flows with either coherence or amplitude based methods (Schaber et al., 1980; Zebker et al., 1987, 1996; Gaddis, 1992; Rowland et al., 2003; Dietterich et al., 2012). They are also commonly used to estimate their thickness and volume, and thus determine volcano extrusion rates (Stevens et al., 1999; Rowland et al., 2003; Terunuma, et al., 2005; Poland, 2014; Bato et al., 2016; Arnold et al., 2017), which is key information in terms of hazard assessment. Interferometry has been used to study the post-emplacement dynamics of lava flows (e.g. Briole et al., 1997; Lu et al., 2005; Ebmeier et al., 2012; Bato et al., 2016; Chaussard, 2016, see table 1), and in turn, calculate their material properties (Wittmann et al., 2017). However, most of these studies were performed on basaltic lava flows emplaced on gentle topographic slopes (see table 1), where lava flows are frequent and InSAR is highly effective. On the contrary, it is well-established that InSAR methods are more difficult to use on andesitic stratovolcanoes because of their steep topography and generally dense vegetation coverage, causing low coherence and noisy data (Pinel et al., 2011). A limitation to the use of InSAR to characterize post-emplacement deformation of lava flows is that, in the absence of additional measurements of the surface displacement such as GNSS or SAR acquired from a different satellite (Peltier et al., 2017), radar images acquired by a given satellite for both the ascending and descending tracks are difficult to use to reconstruct the 3D displacement fields due to the lower accuracy in the north–south (N–S) direction (InSAR measurements being only sensitive to the displacements along the satellite line of sight, which horizontal projection is usually close to the east-west direction for both ascending and descending tracks). Thus, most studies consider that the Line of Sight (LOS) displacements measured result from vertical displacements alone. This assumption prevents the extraction of information about the lava flows horizontal displacement fields being extracted, and could introduce an error into the estimated vertical displacements.

Volcán de Colima, one of the most active volcanoes in North America, is located at the SW front of the Trans Mexican Volcanic Belt (Fig. 1), created by the subduction of the Cocos and Rivera plates under the North American plate. Volcanic activity is characterized by cycles of around one hundred years which culminate in a large Plinian eruption; the last major explosive eruption was in 1913 (Robin et al., 1987; Luhr and Carmichael, 1990).

A new episode of mostly effusive activity began in 1961, when the lava that had slowly infilled the crater left by the 1913 explosions reached the lowest notch in the northern crater rim, generating block-lava flows. Similar episodes of activity followed in 1975-1976 and 1981-1982. In 1991 the lava extrusion began to form a lava dome that fed new block-lava flows (Luhr, 2002). Collapses of the crater rim and the overflowing dome have since caused numerous block and ash flows, particularly in 2004-2005. Dome-building activity resumed in 2007. Vulcanian explosions destroyed the dome in early 2013, and a new dome began growing again overflowing from the crater and producing further lava flows in March 2013 (Capra et al, 2016).

At the end of 2014, an increase in eruptive activity was recorded, notably marked by the July 10 and 11, 2015 pyroclastic density currents (PDCs) which represented the largest runout since 1913 (Capra et al., 2016; Reyes-Dávila et al., 2016; Macorps et al., 2017). The 2015 eruption was not preceded by any detectable precursors in terms of edifice inflation or seismic velocity variations (Lesage et al., 2018). Before and after these events, large lava flows were emplaced on the volcano flanks (Reyes-Dávila et al., 2016). Activity reports describe active lava flows on the western (W) and south–western (SW) flanks from September–November 2014 to mid–February 2015, when no downward motion was observed (Sennert, 2015a). In July, 2015, just after the PDC occurrences, another lava flow formed on the southern (S) flank in the same channel as the PDCs (Sennert, 2015b). Most of studies about this high activity period deal with PDC deposits (Capra et al., 2016; Reyes-Dávila et al., 2016; Macorps et al., 2017) but lava flows should also be considered in order to properly characterize and understand the volcano activity.

The present study combines both radar and optical remote sensing data with the aim of determining where lava flows were emplaced as well as their volumes and their post-emplacement dynamics, in order to have greater insight into the 2014-2015 eruptive crisis of Volcán de Colima. New approaches are proposed to: (1) improve the remote sensing detection of lava flows on andesitic stratovolcanoes, and (2) reconstruct approximate 3D ground displacements associated with the emplacement of lava flows using InSAR LOS measurements on both the ascending and descending tracks from a single satellite, without any other additional observation. Finally, the thermal compaction of the lava flow is numerically modeled and its relative contribution together with the loading and downward flow effect, are investigated. An estimation of the magma bulk viscosity is also derived based on the downward lava displacement.

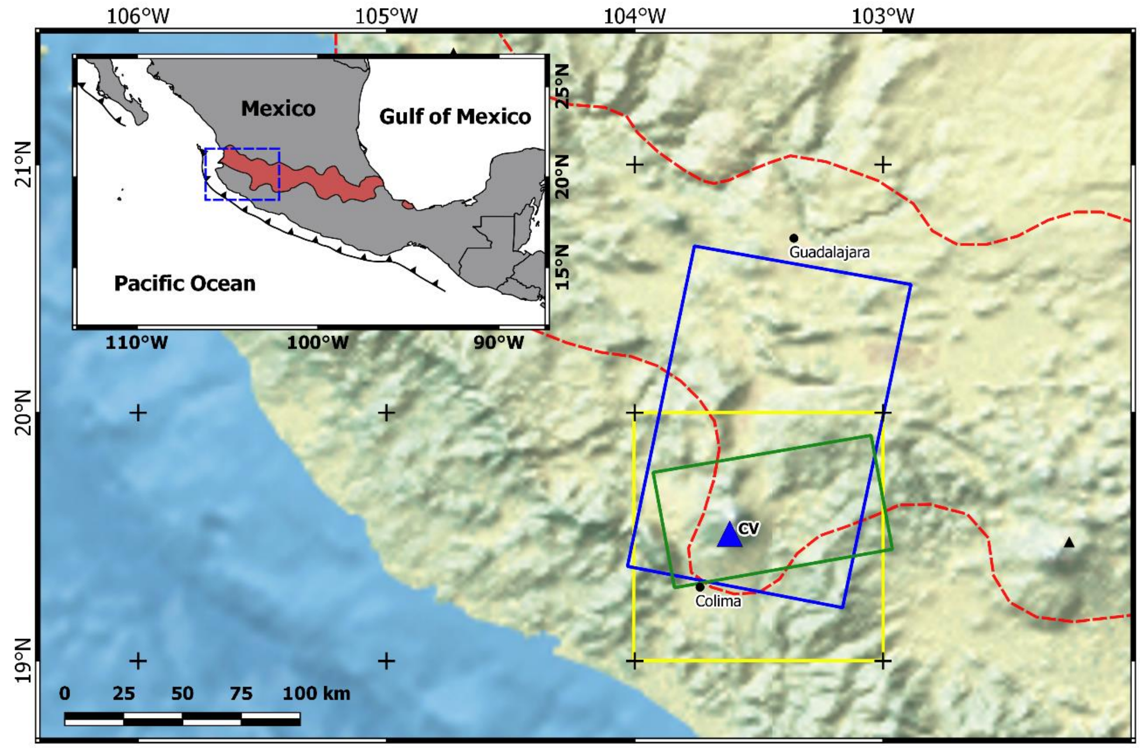

Figure 1: Map with footprints of optical and radar images used in this study. The red dashed line marks the edge of the Trans Mexican Volcanic Belt (TMVB) (red area in the inset). The large blue triangle shows the location of Volcán de Colima (CV). Green and blue rectangles are, respectively, footprints of Sentinel-1A ascending (Orbit A49, sub–swath 3) and descending tracks (Orbit D12, sub–swath 1) (for simplicity, only the bursts and sub–swaths used are delimited). The yellow rectangle delimits the extent of Tandem-X DEM. Inset shows the

described area location (dashed blue rectangle) at a larger scale. The PLEIADES DEM coverage (10×13 km^2 centered on the edifice summit) is not displayed here for clarity.

Volcano (deposit year)	**Time span (yrs)**	**Lava composition**	**Local slope**	**Ref**
Africa				
Fogo (1995)	3	Basaltic	~3°	(Amelung and Day, 2002)
Piton de la Fournaise (1998–2007)	2–16	Basaltic	~17°	(Chen et al., 2018)
(2010)	0.3–3	Basaltic	~7°	(Bato et al., 2016)
Mt Nyamuragira (2004–2010)	0–5.5	Basaltic	~4°	(Samsonov and d'Oreye, 2012)
North America				
Paricutin (1943–1952)	55–68	Basaltic-Andesitic	~5°	(Chaussard, 2016)
(1943–1952)	56–65	Basaltic-Andesitic	~8°	(Fournier et al., 2010)
Santiaguito (2004–2005)	4–6	Dacitic	~21°	(Ebmeier et al., 2012)
Okmok (1958 & 1997)	0.5–3.5	Basaltic	~1°	(Lu et al., 2005)
Colima (1998)	4–8	Andesitic	~25°	(Pinel et al., 2011)
(2014–2015)	0.5–1.1	Andesitic	~18°	This study
Pacaya (2010)	0.1–4	Basaltic	~10°	(Schaefer et al., 2016)
Europe				
Etna (1986–1987 & 1989)	3–7	Basaltic	~23°	(Briole et al., 1997)
(1991–1993)	2–6	Basaltic	~13°	(Stevens et al., 2001)
Krafla (1975–1984)	8–20	Basaltic	~1°	(Sigmundsson et al., 1997)
Hekla (1991 & 2000)	2–25	Basaltic-Andesitic	~8°	(Wittmann et al., 2017)
South America				
Reventador (2002–2005)	3–6	Andesitic	~18°	(Fournier et al., 2010)
Lonquinay (1988–1989)	17–18	Andesitic	~4°	(Fournier et al., 2010)

Table 1: List of the InSAR studies related to lava flow post-emplacement deformations. Local slope was estimated from the SRTM DEM. Time span corresponds to the time lapse between the lava flow emplacement and SAR image acquisition.

2. Data and methods

2.1. Data and processing

Topographic changes induced by lava flow emplacement were estimated based on two Digital Elevation Models (DEM). The pre-eruptive DEM used is the TanDEM-X, 12 m resolution, provided by the German Space Agency (©DLR 2015) and obtained from X-band radar images acquired between January 2011 and August 2014 (see footprint on Fig. 1). A post-eruptive DEM was obtained using one stereo pair of Pleiades optical images (©CNES_2016, distribution AIRBUS DS, France, all rights reserved) acquired on 10 January 2016 and made available through an ISIS (Incitation à l'utilisation Scientifique des Images Spot, French initiative to promote the scientific use of Spot images) project. Pleiades panchromatic images have a nominal resolution of 0.5m. Along-track incidence angles of the two images are -9.3° and -13.1°, while the across-track angle varies between -14.5° and -9.6°. The DEM was computed using the NASA open source software Ames Stereo Pipeline (Broxton and Edwards, 2008). Disparities between the two images are searched for; this provides a point cloud of the surface topography which is then converted onto a grid regularly spaced every 3 m. In this way we obtain a Digital Surface Model, but as no vegetation is present on the region of interest, where lava flows are emplaced, it corresponds to a DEM.

Surface displacements induced by the lava flows were quantified based on 36 SAR images acquired from November 23, 2014 to February 10, 2016, on both ascending and descending tracks, by the European satellite Sentinel-1A with a Vertical-Vertical polarization (Table 2). Images were acquired in Terrain Observation by Progressive Scans SAR (TOPSAR) Interferometric Wide Swath mode (Zan and Guarnieri, 2006) and provided as Single Look Complex (SLC) images with a spatial resolution of 15.6 m in azimuth and 2.3 m in slant range (see Fig. 2 for spatio-temporal distribution of the dataset). As Volcán de Colima’s flanks are steep, local topographic slopes are close to or even greater than the incidence angle, inducing low resolution and a possible layover effect on the flanks facing the satellite. This is particularly true for the descending track where the incidence angle is very close to the volcano slope on the eastern flanks around the summit area (~35°). Ground area affected by low resolution was estimated and consequently masked based on acquisition geometries.

Interferograms as well as coherence images were computed on ascending and descending tracks from SLC images using the NSBAS processing chain as described in Doin et al (2012) and modified to allow for TOPSAR data ingestion (Grandin, 2015). Topographic phase contribution was removed using the SRTM Digital Elevation Model at 30 m resolution oversampled to 15 m. Interferograms were corrected for tropospheric phase delays using atmospheric data provided by the European Center for Medium Range Weather Forecast (ECMRWF) (Doin et al., 2009). Interferograms were then unwrapped using the ROI_PAC branch-cut unwrapping algorithm. Phase delays were converted to LOS ground displacements considering ground displacement as null in a 255x255 m reference area located at the basal part of the SW volcano sector (see Fig. 6–7). Cumulative LOS ground displacements for each successive date after to the first one were obtained by time series inversion, pixel by pixel, using a least squares method (Doin et al., 2012). Lastly, cumulative displacements were geocoded in UTM coordinates on the oversampled SRTM DEM used to correct the topographic phase delay (15×15 m). The time series analysis was performed on a restricted subset of the data to ensure good coherence over the lava flows. As the coherence was too low on lava flows for images acquired before the July eruption (Lesage et al., 2018), we only considered interferograms obtained from images acquired after August 2015 (see Fig. 2B–C).

Date	**Orbite-Slice Sub-swath**	**Date**	**Orbite-Slice Sub-swath**
23 Nov 2014	D12-4 IW1	24 Jul 2015	A49-1 IW3
08 Dec 2014	A49-1 IW3	02 Aug 2015	D12-4 IW1
17 Dec 2014	D12-4 IW1	17 Aug 2015	A49-1 IW3
01 Jan 2015	A49-1 IW3	26 Aug 2015	D12-4 IW1
10 Jan 2015	D12-4 IW1	19 Sep 2015	D12-4 IW1
03 Feb 2015	D12-4 IW1	13 Oct 2015	D12-4 IW1
18 Feb 2015	A49-1 IW3	28 Oct 2015	A49-1 IW3
02 Mar 2015	A49-1 IW3	06 Nov 2015	D12-4 IW1
11 Mar 2015	D12-4 IW1	30 Nov 2015	D12-4 IW1
23 Mar 2015	A49-1 IW3	15 Dec 2015	A49-2 IW3
04 Apr 2015	D12-4 IW1	24 Dec 2015	D12-4 IW1
28 Apr 2015	D12-4 IW1	27 Dec 2015	A49-2 IW3
22 May 2015	D12-4 IW1	08 Jan 2016	A49-2 IW3
06 Jun 2015	A49-1 IW3	17 Jan 2016	D12-4 IW1
15 Jun 2015	D12-4 IW1	01 Feb 2016	A49-2 IW3
30 Jun 2015	A49-1 IW3	10 Feb 2016	D12-4 IW1
07 Jul 2015	D12-4 IW1	25 Feb 2016	A49-2 IW3

Table 2: List of the Sentinel-1A SAR images used in this study. Information on the acquisition geometry for each track is provided in Table 3.

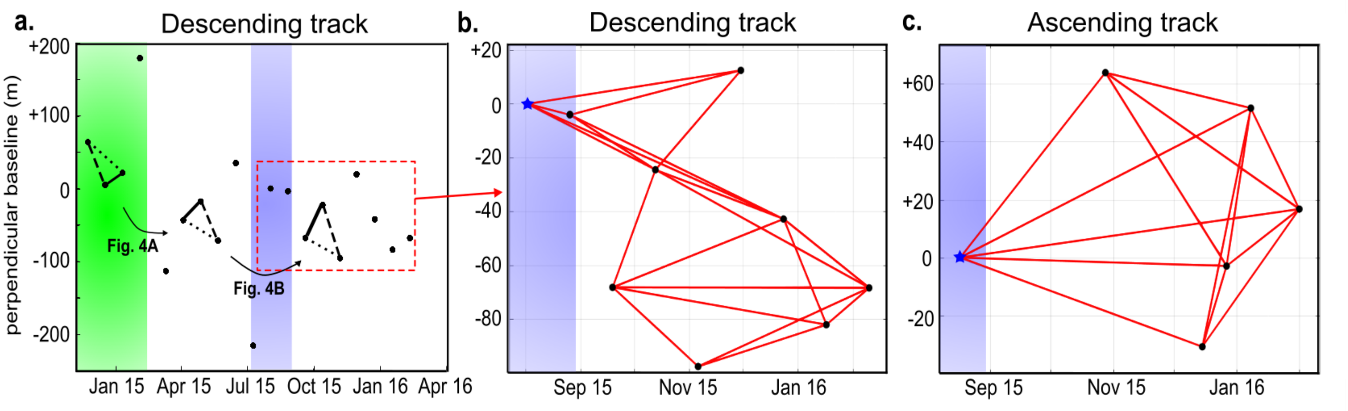

Figure 2: SAR dataset and interferometric networks used **[A]** Spatio-temporal distribution of SAR acquisitions (represented by black dots) for the descending track between November 2014 and March 2016. The green and blue area represent the periods during which the W–SW and S lava flows were reportedly active, respectively. Black lines (respectively solid, dashed and dotted) connect image-pairs with similar temporal and spatial baselines used to quantify the coherence evolution, as shown in Fig. 5. The difference in coherence of each pair of images pair linked by a similar pattern (either solid, dashed or dotted lines) is calculated before averaging the difference in coherence of the three pairs of images (see main text). The dashed red rectangle indicates the spatio-temporal extent of B. **[B]** Subset of descending data used to study lava flow subsidence. Dots are for SAR images (the star being for the master image acquired on August 2, 2015) and red lines are for the 20 computed interferograms. **[C]** Subset of ascending

data used to study lava flow subsidence. Dots are for SAR images (the star being for the master image acquired on August 17, 2015) and red lines are for the 14 computed interferograms.

2.2. Lava flow mapping and thickness estimation

Final lava flow extents and thicknesses were estimated by computing the difference between the DEMs acquired before and after the eruptive deposits emplacement, the TanDEM-X and Pleiades DEMs, respectively. The elevation difference was converted into a thickness (H) of lava emplaced on an inclined substratum using the local slope (α). We estimated the volume of the lava flows as the product of their surface area by average thickness (which is equivalent to the sum of the volume variation of each pixel located on the lava flow). The uncertainty on the DEMs' difference was estimated based on the standard deviation measured on the reference area, which was not affected by any lava flow (empirical estimation as described in Poland, 2014). The uncertainty on the lava flow surface area was estimated by computing the variation resulting from an extension of the lava flow's contours by 1 pixel. Finally, we computed the error on the volume estimations by adding the product of the thickness uncertainty by the lava flow area to the product of the area uncertainty by the average thickness of the lava flow.

In order to gain insight into the timing of lava flow emplacement we used the coherence evolution over the lava flows. The coherence, defined by Zebker and Villasensor, (1992), is a measurement of the similarities in the ground backscattering properties between two SAR images acquired at different dates using both amplitude and phase information. Several sources of decorrelation exist, such as thermal effects affecting the satellite sensor, changes in radar wave penetration which are often induced by vegetation cover, variations in acquisition geometry and temporal decorrelation due to surface and/or topographic changes (Pinel et al., 2014). Our aim was to highlight the coherence evolution due to surface changes by reducing the effects of other decorrelation sources. The summit area of Volcan de Colima (~5 km around the crater) is free of vegetation, thus the main sources of decorrelation are geometric effects, thermal noise, and surface changes, mostly induced by the emplacement of volcanic deposits. Lee and Liu (2001) showed that the geometric decorrelation related to terrain slope is proportional to the perpendicular baseline between the two images. It follows that couples of images with similar temporal and spatial baselines are theoretically affected by the same loss of coherence. In order to reduce the influence of geometric decorrelation, we selected, for three different periods, several image pairs with similar temporal and perpendicular baselines (Fig. 2A). Comparison of these pairs thus highlight surface changes, with possible contribution of thermal sensor noise. The selected periods are during the deposition of the W and SW flank lava flows (no data were available before), after their deposit, and after the occurrence of the July 2015 crisis, respectively. For each period, we computed the coherence for the various image-pairs. Then, we compared, for given successive periods, the coherence difference for couples with the same temporal and perpendicular baselines. As coherence data are very noisy in the summit area of Volcan de Colima , we average the coherence differences computed for given successive periods in order to highlight surface changes resulting from lava flow emplacements rather than noise induced by frequent ash emissions (Pinel et al., 2011) and thermal sensor effects.

2.3. Reconstruction of 3D ground displacement field

For each track, calculated ground displacements are 1D and correspond to a projection of the displacement vector in the satellite Line Of Sight (LOS) direction. Therefore, at least three independent measurements with different acquisition geometries are required to reconstruct the displacement vector in 3D (Wright et al., 2004). In most cases, only two distinct measurements (right-looking ascending and descending paths) are available, so that the problem is underdetermined. Having additional geometry of acquisitions clearly improves the accuracy of the retrieved 3D displacement (Peltier et al., 2017). However, due to the near-polar satellite orbit, the N–S component of the displacement is always less well constrained. One method commonly used in volcanology is then to assume a null displacement in the NS direction and to invert for the vertical and E–W displacement (Samsonov et al., 2017). The flaw in this approach is that the orientation of the horizontal displacement field is strongly dependent on the displacement source and cannot necessarily be neglected in the N–S direction. Here, we favor an alternative approach for which we use a strong *a priori* based on a physical model to fix the orientation of the horizontal displacement. As we study lava flows, we follow a strategy similar to the one used in glaciology. In order to quantify mass sliding of glaciers from InSAR measurements, authors often make the assumption that, when there is a horizontal component of displacement, it will be directed down the maximum slope (e.g. Rabus and Fatland, 2000). Thus, the problem becomes bi-dimensional and the displacement vector can be estimated using both ascending and descending LOS displacement measurements. As a lava flow path is mainly controlled by the topography (Felpeto et al., 2001; Mossoux et al., 2016), the same assumption can be made for lava flows by considering that, if a bulk horizontal motion is observed, it should be aligned with the direction of maximum slope.

In the next section, the angles on the horizontal plane are defined relative to the east and are considered positive in a counterclockwise sense. On E–W and N–S components, displacements are defined as positive towards the E and N, respectively. Vertical motions are considered positive in the upward direction (Fig. 3A). On each track, the displacement measured, d^{LOS}, is a projection of the displacement vector, *d*, in the LOS direction:

$$d^{LOS} = d\,\hat{p}, \tag{1}$$

where $\hat{p}$ is the unit LOS vector, pointing from the satellite to the ground. Using θ, the satellite look angle, and ϕ the horizontal angle between satellite LOS directions and E direction (which is opposite to the heading defined as the direction of the satellite trajectory relative to the north, positive in a clockwise sense, provided in SAR images metadata and noted as ϕ' in Fig. 3B and Table 3, ϕ =- ϕ'), $\hat{p}$ can be expressed in three dimensions on the N, E and V directions by $\hat{p}_N, \hat{p}_E$ and $\hat{p}_V$:

$$\hat{p} = \begin{cases} \hat{p}_N \\ \hat{p}_E \\ \hat{p}_V \end{cases} = \begin{cases} sin\,\phi\,sin\,\theta \\ cos\,\phi\,sin\,\theta. \\ -\,cos\,\theta \end{cases} \tag{2}$$

A rotation, in the horizontal plan, of the coordinate system by an angle α is introduced (Fig. 3B). This angle corresponds to the maximum slope direction, relative to the E, direction along which the lava is expected to flow. The normal vector $\hat{p}_N$ and $\hat{p}_E$ are thus transformed in $\hat{p}_L$, the normal vector oriented towards the maximum slope and $\hat{p}_T$, the transversal direction of $\hat{p}_L$:

$$\hat{p} = \begin{cases} \hat{p}_N \\ \hat{p}_E \\ \hat{p}_V \end{cases} => \hat{p} = \begin{cases} \hat{p}_L \\ \hat{p}_T \\ \hat{p}_V \end{cases} = \begin{cases} cos\,\phi\, sin\,\theta\, cos\,\alpha + sin\,\phi\, sin\,\theta\, sin\,\alpha \\ sin\,\phi\, sin\,\theta\, cos\,\alpha - cos\,\phi\, sin\,\theta\, sin\,\alpha \\ - cos\,\theta \end{cases} . \tag{3}$$

Then, we assume the lava flows displacements as null in the transversal direction (This requires to consider that lateral spreading motions are negligible compared to the displacement in the maximum slope direction). Thus, the problem becomes 2D and by using the geometrical parameters of the acquisitions ($\hat{p}_L$ and $\hat{p}_V$), and LOS displacements, on both tracks (Ascending and Descending), the equation set can be formulated as:

$$\begin{bmatrix} d_{asc}^{LOS} \\ d_{des}^{LOS} \end{bmatrix} = \begin{bmatrix} \hat{p}_{L_{asc}} & \hat{p}_{V_{asc}} \\ \hat{p}_{L_{des}} & \hat{p}_{V_{des}} \end{bmatrix} \begin{bmatrix} d_L \\ d_V \end{bmatrix}, \tag{4}$$

which can be solved to retrieve d_L and d_V, the displacements along the maximum slope and vertical directions, respectively:

$$\begin{bmatrix} d_L \\ d_V \end{bmatrix} = \begin{bmatrix} \hat{p}_{L_{asc}} & \hat{p}_{V_{asc}} \\ \hat{p}_{L_{des}} & \hat{p}_{V_{des}} \end{bmatrix}^{-1} \begin{bmatrix} d_{asc}^{LOS} \\ d_{des}^{LOS} \end{bmatrix}. \tag{5}$$

Eventually, displacement d_L is re-expressed in the N and E directions in order to represent the solution on a map:

$$d = \begin{cases} d_N \\ d_E \\ d_V \end{cases} = \begin{cases} d_L\, sin(\alpha) \\ d_L\, cos(\alpha) \\ d_V \end{cases} . \tag{6}$$

Geometrical parameters of the ascending and descending acquisitions are indicated in Table 3. The maximum slope direction is computed from the TanDEM-X DEM, the most recent prior to the lava flow emplacement, down-sampled at 60 m in order to reduce potential DEM error effects. For each pixel covered by both tracks, we used Eq. 5–6 with the local maximum slope direction to obtain a map of vertical and horizontal displacements.

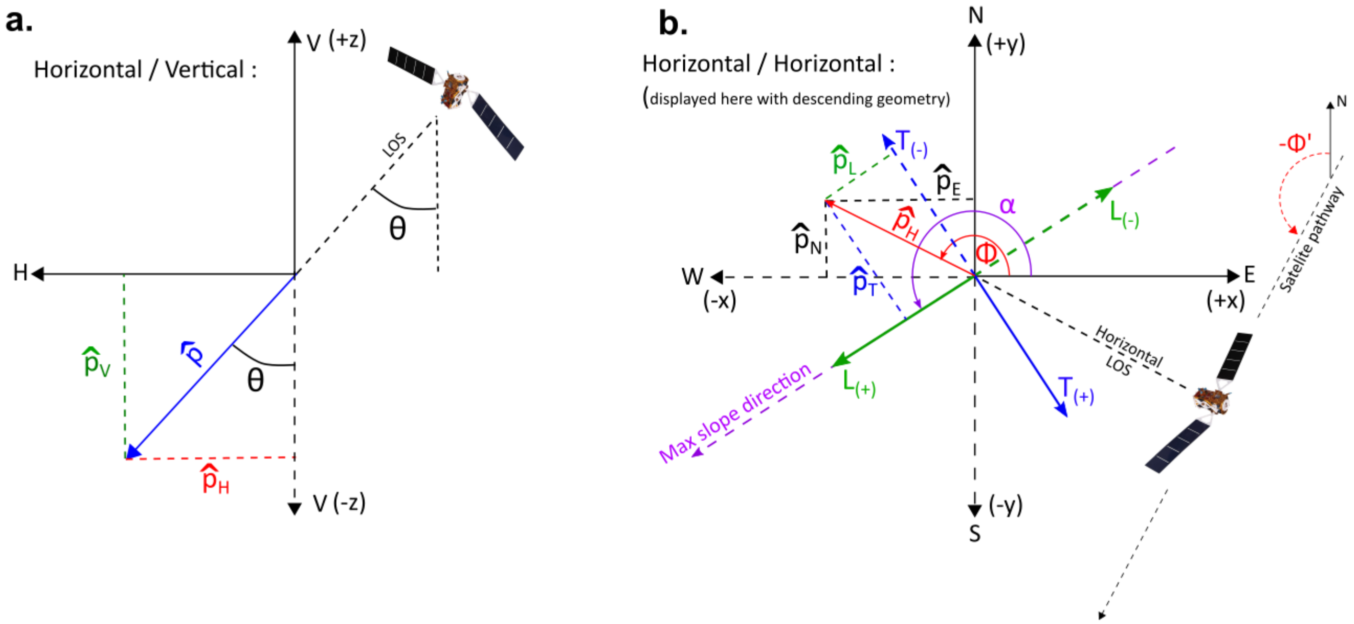

Figure 3: Schematic diagram of the reference system considered when reconstructing an approximate 3D displacement field. **[A]** Horizontal/Vertical plan representation of the satellite acquisition geometry. **[B]** Horizontal/Horizontal plan representation. Explanations about the vectors, axes and variables plotted can be found in the text.

Acquisitions	**Angles**
Descending track	ϕ' = -167.78°
(D12,IW1)	Θ = 34.10°

Ascending track	ϕ' = -12.19°
(A49,IW3)	Θ = 43.97°

Table 3: Satellite acquisition geometries with angles used to reconstruct the 3D displacement field. ϕ' is the heading corresponding to the satellite pathway orientation relative to the North (positive in a clockwise direction), and θ is the angle of incidence.

3. Results derived from remote sensing dataset

3.1. Lava flow mapping and volume estimations

Figure 4A displays the DEM difference between the TanDEM-X and the Pleiades DEMs. It shows four distinct areas where topographic changes are significant, located on the northern (N), W, SW and S flanks. All these areas are consistent with lava flow emplacement as detailed by Reyes-Dávila et al., (2016). We used the DEM difference to delimit and precisely map the lava flows. The average thicknesses of the W and SW lava flows are 17.3 ± 1.5 m and 19.3 ± 1.5 m, with maxima of 51.5 ± 1.5 m and 65.4 ± 1.5 m, respectively. We estimated their volumes to 5.04 $\pm 0.38 \times 10^6$ m^3 (W) and $13.13 \pm 0.52 \times 10^6$ m^3 (SW). It is challenging to estimate precisely the thickness and volume of the lava flow on the S flank because it was emplaced onto the same path as the PDCs, which can result in both deposition of materials and edifice erosion. The amount of materials removed from the summit during the July 2015 events is estimated at 3.83 $\pm 0.26 \times 10^6$ m^3.

As the time between the two DEMs used to estimate elevation changes is more than 18 months, we use the coherence evolution to further constrain the timing of lava flow emplacement. Figure 5 shows the coherence evolution maps for the two periods analyzed. Both maps present noisy results, but some significant evolutions in the coherence can be seen. Between approximately December 2014 and April 2015, a significant increase of the coherence is observed on the SW and W (Fig. 5A), where active lava flows had been reported until February 2015 (Sennert, 2015a). This result shows that, in May 2015, a large part of the SW and W lava flows had already recovered a good coherence suggesting limited displacement at their surface. No coherence change is detected on the N flank, suggesting that part of the N lava flow had been emplaced prior to this and it was thus not contemporaneous with the emplacement of the SW and W lava flows. The second coherence map (Fig. 5B), covering the time lapse between April and October 2015, presents an additional increase in coherence on the SW lava flow mainly in its lower part, corresponding to the thickest cross-section of lava (see Fig. 4A). Results on the W lava flows are less obvious but we observed a coherence increase at a localized area in the upper part, also where lava thickness is expected to be greater. This is consistent with the observation on basaltic lava flows made by Dietterich et al., (2012), that the time required for a lava flow to become coherent increases with the lava thickness. This behavior is probably related to the fact that the amplitude of the displacement observed on lava flows is in proportion to the lava thickness such that it takes more time for the horizontal displacement to decrease below a threshold at which there is a coherence stability when the lava is thicker. We also notice that a loss of coherence affects the area where PDCs and the S lava flow were emplaced in the summer of 2015 (Fig. 5B).

We used the volume of the W and SW lava flows, which were emplaced contemporaneously, to estimate a mean extruding rate of 1-2 m^3 s^{-1} between November 2014 and February 2015. We have not taken into account the small volume (< 2×10^6 m^3) of the N lava flow on the coherence map, as its emplacement timing is not well constrained implying that the estimated extrusion rate might be slightly underestimated.

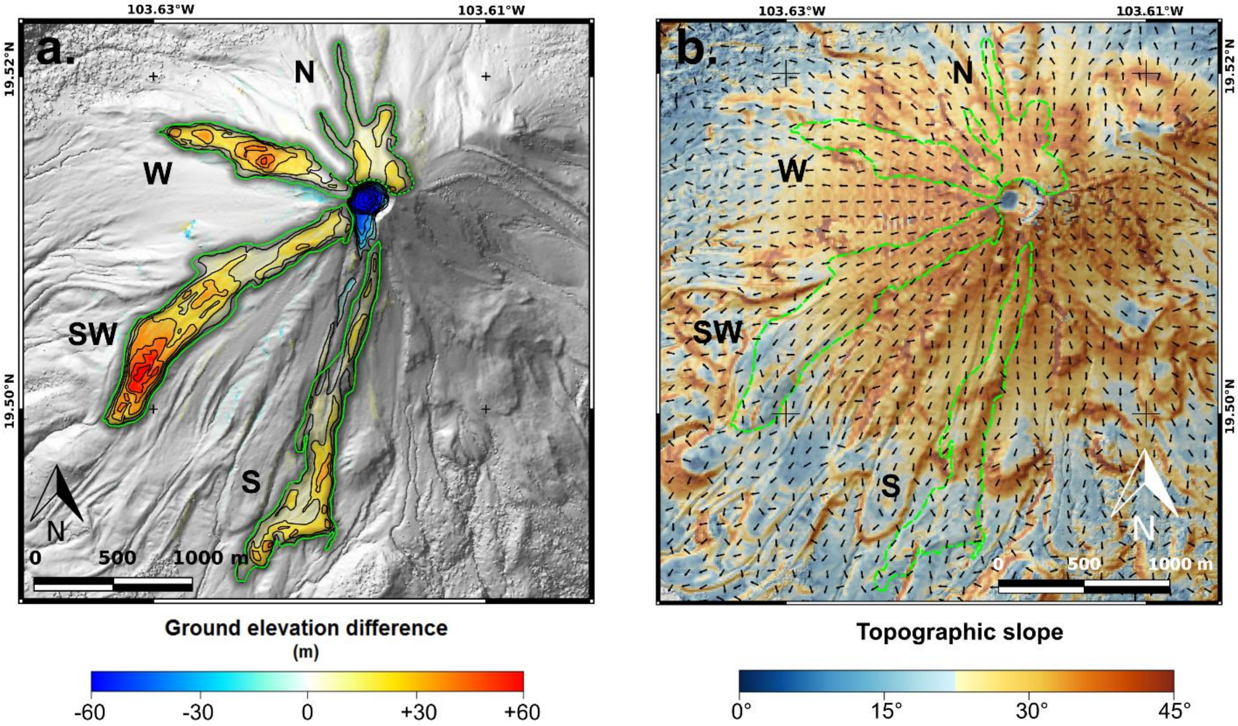

Figure 4: Deposit thickness and Volcán de Colima slope **[A]** Vertical difference between the TanDEM-X and Pleiades DEMs acquired, respectively, from 2011 to 2014 and in January 2016. Green lines are for lava flow edges derived from elevation changes. Black lines display thickness contour with an interval of 10m. **[B]** Local topographic slope (the local orientations of maximum slope are indicated with short black lines) computed from the TanDEM-X DEM.

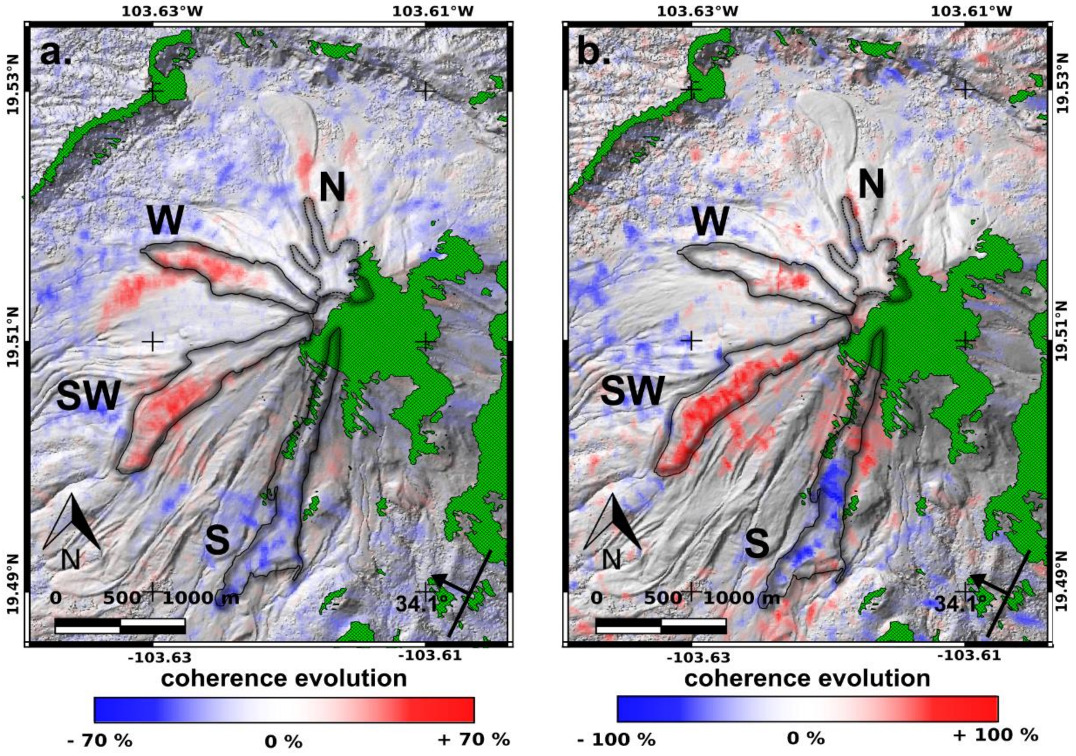

Figure 5: Average coherence evolution between December 2014 and April 2015 **[A],** and April 2015 and October 2015 **[B]**. Green areas represent locations with low resolution or layover effect. Contour of lava flows, plotted as black lines, are defined based on DEM difference (see Fig. 4A).

3.2. Average ground displacement rates

Figure 6 presents the average LOS displacement rates, in mm yr^{-1}, measured on both ascending (A) and descending (B) tracks, between August 2015 and February 2016. Both tracks cover the SW lava flow whereas the W deposit is only observed on the descending track and the S flank deposits (lava flow and PDCs) are better imaged on the ascending track. The signal recorded on all deposits is always consistent with a displacement away from the satellite in the LOS. This is the case for the SW and W lava flows and also for the S flank where the lava flow and the PDCs are located (Capra et al., 2016; Reyes-Dávila et al., 2016; Macorps et al., 2017). We now focus on the SW lava flow, which is the only one where displacements are well imaged on the two available tracks. The average displacements rates, away from the satellite, are 64 ± 8 mm yr^{-1} and 82 ± 8 mm yr^{-1} on ascending and descending tracks, respectively. The maximum displacement rates are 128 ± 8 mm yr^{-1} and 176 ± 8 mm yr^{-1}, located on the lava flow. We note that on the descending track, a sharp decrease in the LOS displacement rate is observed when moving towards the summit along the lava flow. This sharp decrease occurs at the exact location of the abrupt slope change from ~35° on the summit part to ~20° on the basal part (Fig. 4B), and just above the thickest part of the lava flow (Fig. 4A). We hypothesize that this reflects locally complex behavior of the lava flow with an expected piling up of the material at the slope failure.

We estimated the 3D displacement field on the pixels covered by both tracks with Eqs. 5–6. The parameters, $\hat{p}$, of both tracks were computed with the acquisition geometries reported in Table 3 and local topographic slopes, α. Figure 7A presents the vertical displacement rates obtained for each pixel covered by both tracks, and Fig. 7B is a zoom of the SW lava flow with the associated horizontal displacements. On the SW lava flow, the estimated mean vertical displacement rates are 129 ± 9 mm yr^{-1} with a maximum of 182 ± 9 mm yr^{-1}. Results show clear horizontal motion located within the flow area, with an average velocity of 26 ± 11 mm yr^{-1} and a maximum of 63 ± 11 mm yr^{-1} located where the topographic slope is maximal. Towards the flow front, the average horizontal displacement decreases to about 20 ± 11 mm yr^{-1}. These results highlight that the lava flow still has a downward flow motion despite the fact that it had been reported as emplaced in February 2015 (Sennert, 2015a). Note that this horizontal displacement is small enough to ensure a coherence stability over the 7 month period studied.

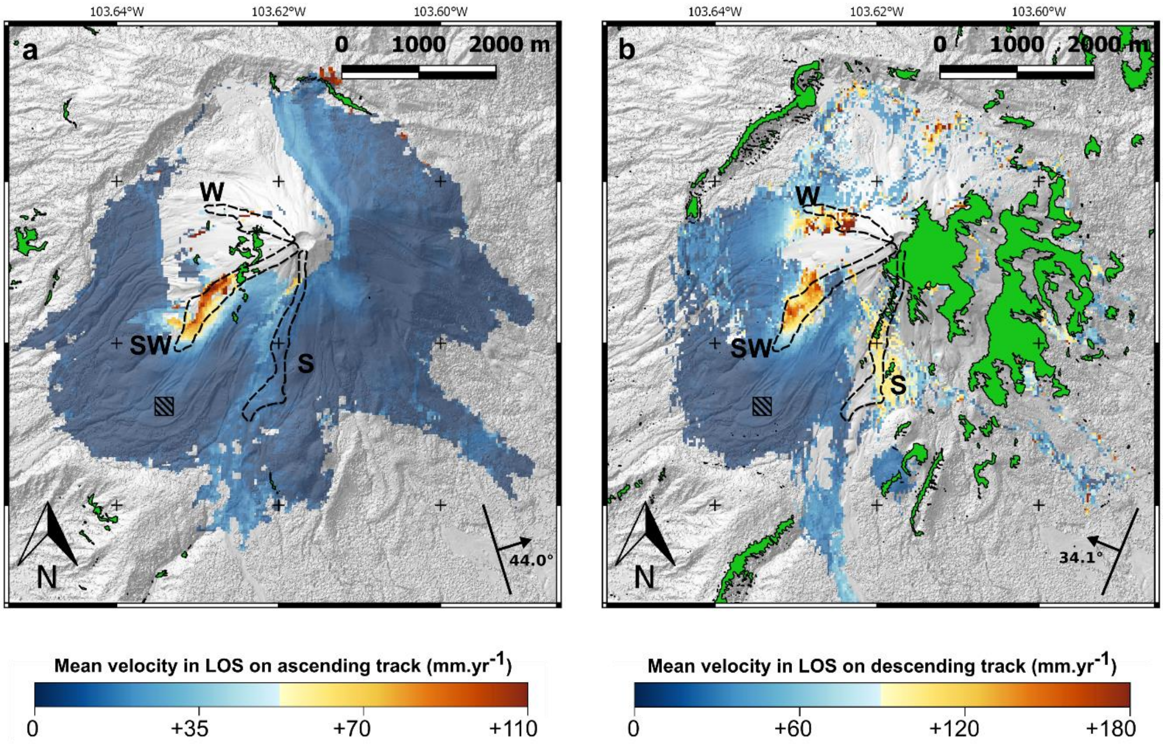

Figure 6: Average LOS displacement rate observed from August 2015 to February 2016 on ascending **[A]** and descending **[B]** tracks. Displacements are positive away from the satellite (along the unit LOS vector $\hat{\mathrm{p}}$ as defined by Eq. 3). Dashed black lines mark the extent of W, SW and S lava flows. The hatched square is the reference area where displacements were assumed to be null. Green areas are for locations with low resolution or layover effects.

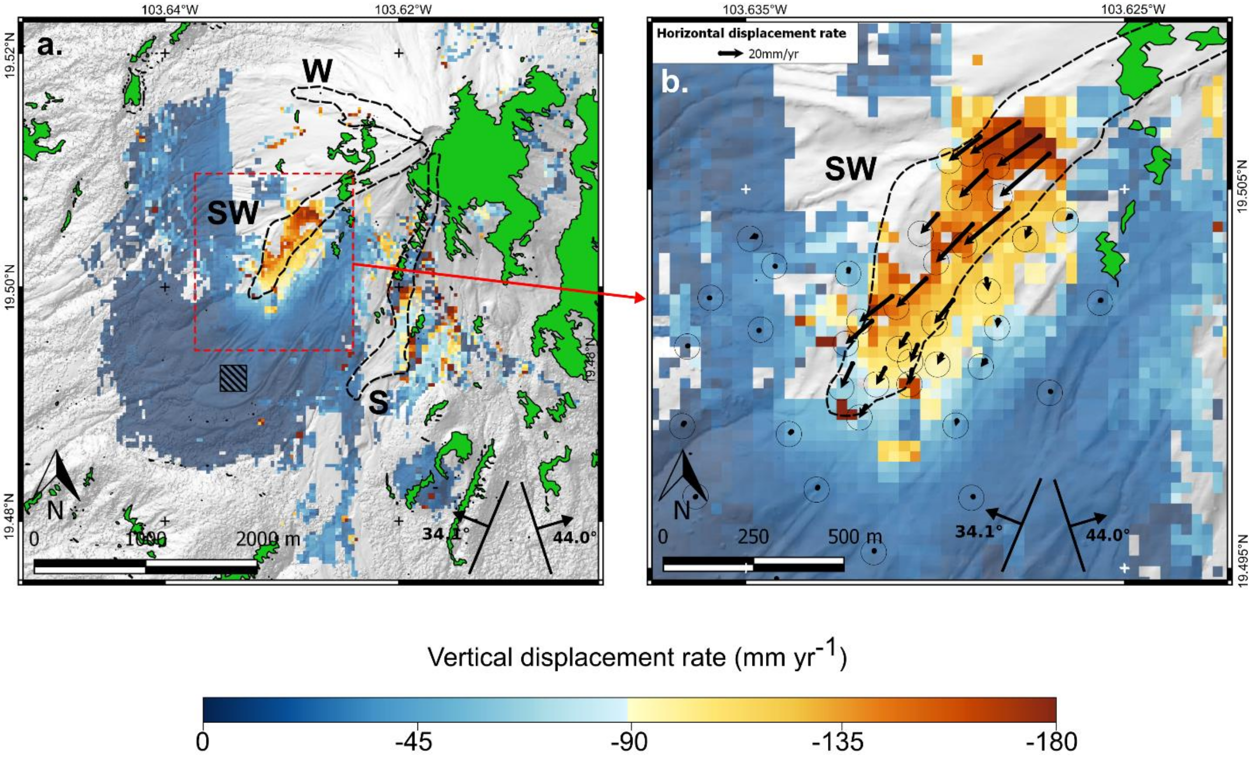

Figure 7: 3D displacement field of the SW lava flow **[A]** Mean vertical displacement rate (from August 2015 to February 2016). Positive values are for an upward displacement. Green areas represent places affected by very low resolution or layover on both tracks. The hatched square is the reference area where displacements are assumed to be null. The red rectangle shows the extent of the zoom displayed in Fig.7B. **[B]** Zoom of the SW lava flow with horizontal motion vectors. Circles represent the uncertainties on displacement vectors. Dashed black lines mark the edges of lava flows derived from DEMs difference. Note that whereas the horizontal displacements are negligible outside the lava flow, the vertical ones remain significant around the lava flow due to loading effects.

3.3. Temporal evolution of ground displacements

We selected 87 points located on the SW lava flow covered by both ascending and descending tracks (Fig. 8A). No point was taken from within the area where the sharp decrease of LOS displacement rate was observed (Fig. 7), due to the complexity of the lava flow behavior in this area and the uncertainty on the local slope. We computed the LOS displacement rate between consecutive acquisition dates for each point (taking the displacement difference divided by the temporal baseline) and normalized this value using the local deposit thickness following Ebmeier et al., (2012). The temporal evolution of the displacement rate was then fitted for each point using a 1st degree polynomial for the ascending tracks and a 2nd degree polynomial for the descending ones, according to the observed trend. Finally, we computed average temporal evolution curves for each track over all points sampled (indicated by thick curves in Fig. 8B). The error on the average curves, for each date, is given by the distance between minimum and maximum values. Results are presented in Fig. 8B. For the descending track, the average LOS displacement rate decreases from 4.2 ± 1.2 mm yr^{-1} m^{-1} in August 2015 to 2.0 ± 0.7 mm yr^{-1} m^{-1} in February 2016. For the ascending track, the average LOS displacement rate is almost constant between August 2015 and February 2016 with a value of 1.6 ± 0.6 mm yr^{-1} m^{-1}. The displacement rate measured on the descending track thus decreases with time, as commonly observed on lava flows affected by subsidence (Chaussard, 2016) whereas there is almost no temporal evolution of the displacement measured on the ascending track. The difference in behavior between the two tracks can be explained when considering horizontal displacements shown on Fig. 7B. The ascending and descending tracks have different sensitivities to horizontal motion along the maximum slope direction. The descending LOS, being nearly perpendicular to the flow direction, is almost insensitive to horizontal displacements. Thus, displacements recorded on this track reflect principally vertical deformation. On the contrary, the ascending track is aligned with the lava flow and is thus sensitive to horizontal displacement. The fact that the vertical displacement decreases with time, as shown on the descending track, together with the constant displacement rate measured on the ascending one, results from a combination of vertical and horizontal motion, and must imply that the horizontal displacement rate also decreases through time.

In order to confirm this observation, we adopted the same approach as above to reconstruct the 3D displacement field (Fig. 7 and Eqs. 6–7). The sampling points are characterized by their average thickness, topographic slope, and average LOS displacements. Figure 8C displays the results for the temporal evolution of vertical and horizontal (along the maximum slope direction) displacements. We thus verify that displacement rates decrease with time on both the vertical and horizontal components. The vertical subsidence rate goes from 4.4 ± 0.9 mm yr^{-1} m^{-1} in August 2015 to 2.7 ± 0.9 mm yr^{-1} m^{-1} in February 2016, and the horizontal one decreases from 2.2 ± 1.1 mm yr^{-1} m^{-1} to -0.3 ± 1.1 mm yr^{-1} m^{-1} (positive values corresponding to a displacement directed towards the front of the lava flow).

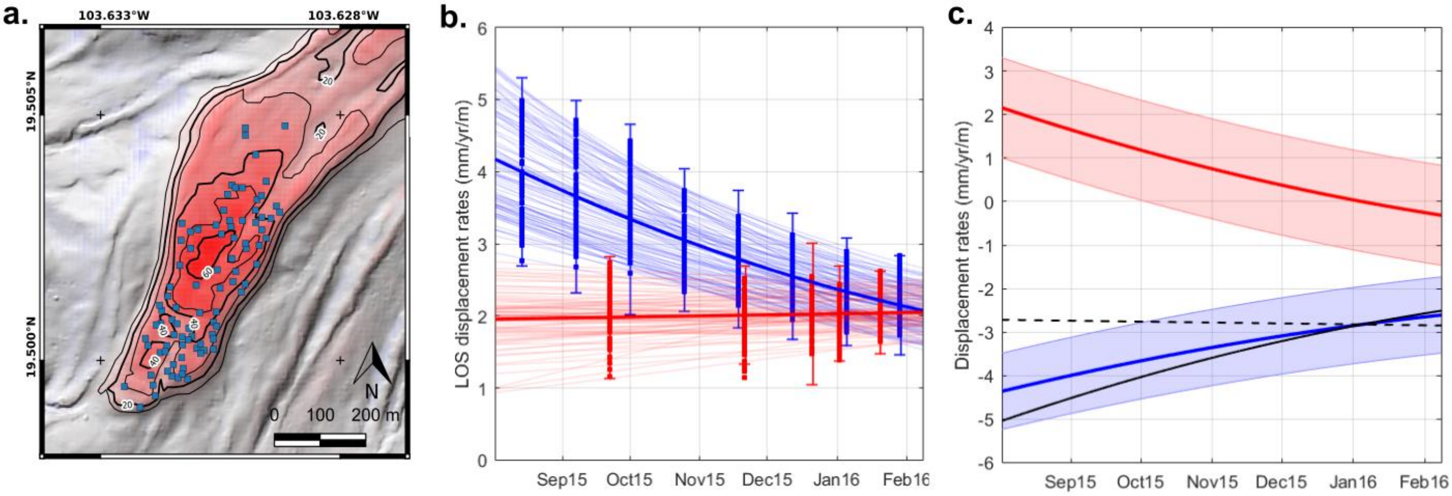

Figure 8: Evolution of the post-emplacement ground displacement **[A]** Positions of the sampling points located on the SW lava flow (blue squares). Contour lines indicate the lava flow thickness measured by DEM differences (Fig. 4A). **[B]** Temporal evolution of the post-emplacement LOS displacement rates (in red for the ascending track and in blue for the descending one, positive values away from the satellite). Displacement rates measured between two successive images at sampling points are indicated by squared symbols. Thin curved lines correspond to the fit performed for each point. Thick curved lines are the fit of displacements rate obtained by averaging all the sampling points. **[C]** Temporal evolution of the vertical (in blue, negative values for downward displacement) and horizontal (in red, positive values for displacement towards the front of the lava flow) post-emplacement displacement rates and associated uncertainties. This information is derived from the averaged post-emplacement LOS displacement rate presented in Fig. 8B and the average substratum slope and orientation at the sampled points. The solid and dashed black curves indicate the vertical displacement rates retrieved assuming

no horizontal displacements (applying Eq. 9) on the descending and ascending tracks, respectively.

3.4. Numerical modeling of the lava thermal contraction

A significant part of the displacement recorded on lava flows is expected to be caused by thermal contraction of the lava. After its emplacement, the lava flow cools, with diffusion of its heat into the substratum and the ambient air, inducing both contraction of the lava flow and expansion of the substratum. Thermal contraction of the lava flow induces displacements mainly on the vertical component, but also on the horizontal one, in the summit direction, because of the topographic slope (see Fig. 9A). To estimate the thermo-elastic contribution of the recorded displacements, we carried out numerical modeling of the lava flow cooling and induced deformations using a Finite Element Method (FEM). The cooling model is a simplified version of the one proposed by Patrick et al., (2004), and used by other studies to model thermal contraction of lava flows (Chaussard, 2016; Wittmann et al., 2017). It consists of an upper lava flow layer, of thickness H, emplaced on a substratum inclined at an angle α (Fig. 9A). At the interface between lava and air, the heat is exchanged by both radiation and convection. Within the lava flow and into the substratum, the heat is assumed to be transferred only by conduction. Initial temperature profile and typical simulation result are reported in Fig. 9B. The temperature evolution of the elements induces their deformation. We take into account the contraction of the lava flow, due to cooling, and also the expansion of the heated substratum. As the model is 1D, the relationship between volumetric and linear compaction must to be taken into account by involving the Poisson coefficient (Chaussard, 2016; Wittmann et al., 2017). Key points of the FEM implementation are given in the Supplementary Material SIA.

The morphology of the SW lava flow, is characterized by its short length and steep edges, and is similar to flows reported on Merapi volcano (Indonesia) by Voight et al. (2000), where lava tongues are fed by lava dome material extruded on the flank. We thus assume that the materials emplaced in such flows has the same composition and properties as the dome itself. This is confirmed by lava blocks collected on similar active lava flows, at Volcán de Colima (Savov et al., 2008). The collected samples present low porosity probably due to degassing during the slow ascent of the emplaced material through the conduit (Lavallée et al., 2012; Cassidy et al., 2015). During its ascent and evolution inside the dome itself, the magma cools and crystallizes as highlighted by the high SiO_2 composition of glass in the dome clasts collected at Volcán de Colima (Cassidy et al., 2015). As degassing and crystallization is already at an advanced stage before lava flow emplacement, the vesiculation and latent heat effects during the cooling of the lava flow are neglected in this study.

We assumed the lava flow and substratum to be of the same composition with their conductivities, heat capacities and densities being only functions of the temperature. We adopted the same approach as Patrick et al. (2004) to estimate the temperature dependence on the thermal conductivity (*k*) for andesitic lavas. A fit of the conductivity measured on Mt Hood (USA) andesite by Murase and McBirney, (1973), leads to the following relationship :

$$\begin{cases} T < 1073K & k(T) = -3.3754 \times 10^{-4}\, T + 1.4721\, W\, m^{-1}\, K^{-1} \\ T \geq 1073K & k(T) = 7.6677 \times 10^{-4}\, T + 0.2874\, W\, m^{-1}\, K^{-1} \end{cases} . \qquad (7)$$

The temperature dependence on the lava heat capacity is implemented in the same way as for other lava flow cooling models (Patrick et al., 2004; Chaussard, 2016). Finally, the local density evolution is computed based on the lava thermal expansion coefficient, β, as

$$\rho(T) = \rho_{ref}\left(1 + \beta\left(T - T_{ref}\right)\right). \tag{8}$$

The thermal expansion coefficient is a key parameter that controls the lava flow thermal contraction rate. Its values depend on several properties of the rock, such as temperature, crack content, porosity, composition and history (Richter and Simmons, 1974; Bauer and Handin, 1983). As no *in situ* measurements of the emplaced material are available, we used two end members values from the literature (Murase and McBirney, 1973; Bauer and Handin, 1983; Mallela et al., 2005). The lowest value is taken at $\beta=1.0 \times 10^{-5}$ K^{-1}, and the maximum at $\beta=3.5 \times 10^{-5}$ K^{-1}. The physical parameters considered in the model are summarized in Table 4. The starting date of the simulation (t_o) was chosen to be the middle of the deposition period between the time when the lava flow started and the time when it was reported to be emplaced (after the supply rate had ceased). This parameter cannot be more precisely estimated here, but its influence on the predicted displacement rates decreases as time increases from t_o. As the InSAR time series starts several months after the emplacement time, the uncertainty on this initial time has a limited impact on the results of the modeled displacement velocity (less than ±5% here if the starting date is moved by one month before or after the selected date used here).

Results of the numerical modeling, on the time lapse analyzed by the InSAR time series, illustrate that thermal compaction of the lava flow produces displacement in both vertical and horizontal directions (Fig. 10A). Not surprisingly, the estimated displacement rate, produced by thermo-elastic contraction, is strongly affected by the value of the thermal expansion coefficient. With the maximum value, β=3.5 × 10^{-5} K^{-1}, the predicted vertical displacement rate, in the downward direction, is 134.2 mm yr^{-1} in August 2015, and decreases to 98.4 mm yr^{-1} in February 2016. The associated horizontal displacement rates at these dates are 44.8 mm yr^{-1} and 32.9 mm yr^{-1} in the summit direction, respectively (Fig. 10A). When the thermal expansion coefficient is β=1.0 × 10^{-5} K^{-1}, the vertical subsidence rate decreases from 38.0 mm yr^{-1} to 28.0 mm yr^{-1} between August 2015 and February 2016. The corresponding horizontal rates are 12.7 mm yr^{-1} and 9.3 mm yr^{-1}, respectively, towards the summit.

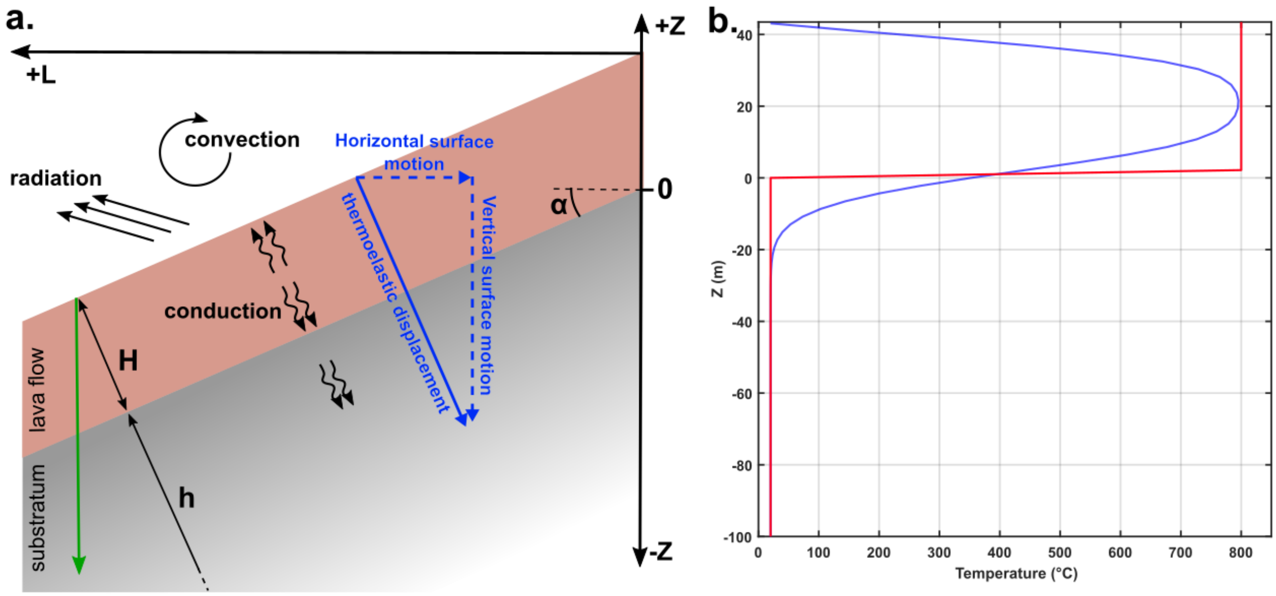

Figure 9: Lava flow cooling and contraction using numerical modelling **[A]** Conceptual model used for thermal contraction. The solid blue vector indicates the expected surface displacement associated with thermo-elastic compaction. The dashed blue vectors represent its projection on the vertical and horizontal directions. The green arrow corresponds to the 1D direction

considered in the numerical model and to the section represented in Fig. 9B. **[B]** Vertical distribution of the temperature at initial conditions (red curve), and after 2 years of cooling (blue curve).

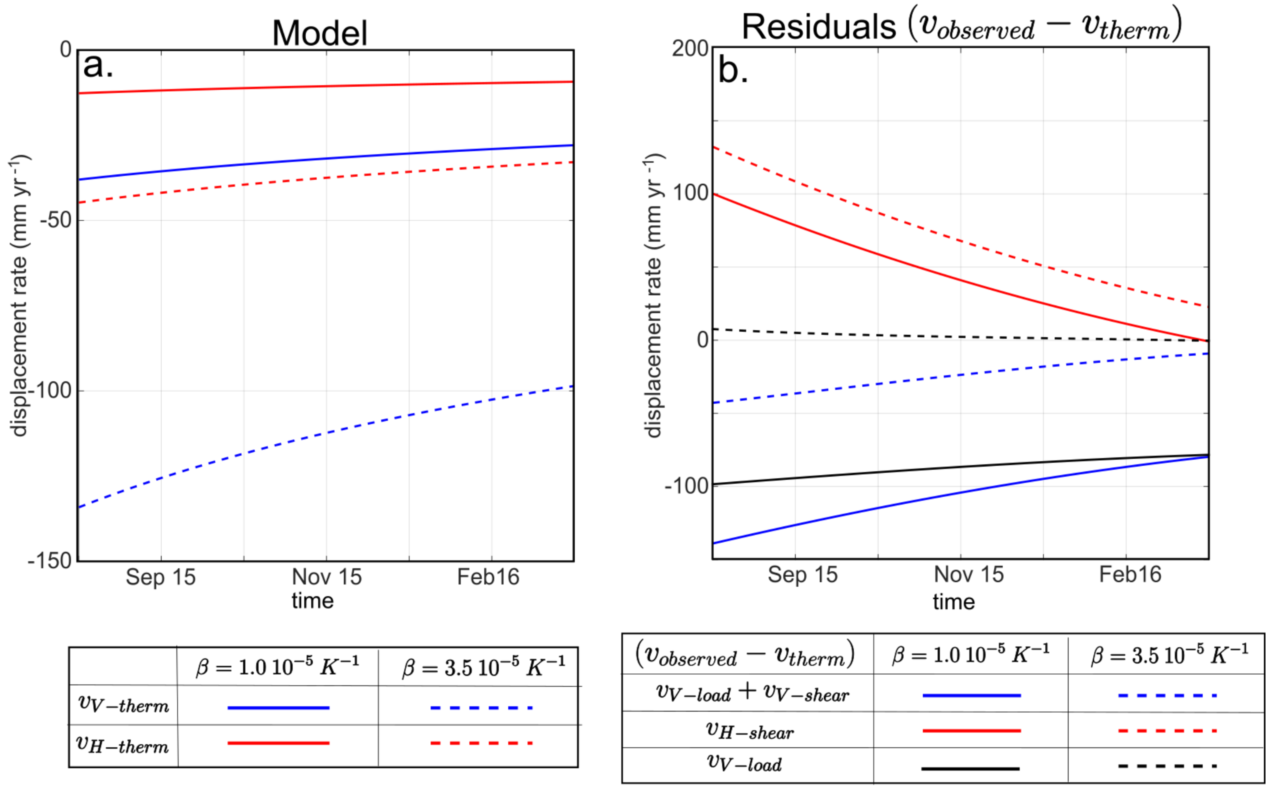

Figure 10: Lava flow thermal contraction results. **[A]** Surface displacements predicted by the numerical modeling induced by lava thermo-elastic contraction in vertical ($v_{V-therm}$: blue curve, positive upward) and horizontal ($v_{H-therm}$: red curve, positive towards the lava flow front) directions during the time period covered by the InSAR time series. The solid and dashed lines are obtained using different end-members for the value of the thermal expansion coefficient: 1×10^{-5} K^{-1} and 3.5×10^{-5} K^{-1}, respectively. **[B]** Residual displacement rates obtained after removing the modeled thermo-elastic contraction from the InSAR measurements (blue and red curves for the vertical and horizontal components, respectively). Black curves represent the residual vertical displacement rate corrected for the vertical component $v_{V-shear}$ of the flow shearing effect ($v_{V-shear} = \tan a\, v_{H-shear}$, with α the flank slope set at 20.9°). The solid

and dashed lines, respectively, are obtained using different end-members for the value of the thermal expansion coefficient: 1×10^{-5} K^{-1} and 3.5×10^{-5} K^{-1}, respectively.

Parameter	**Model input (Units)**	**Reference**
Geometrical parameters		
Lava flow thickness : H	40.6 m	This study
Substratum thickness	100 m	-
Substratum tilt	20.9°	This study
Physical parameters		
Air dynamic viscosity : η_a	1.725×10^{-5} Pa s	-
Air heat capacity : Cp_a	1006 J kg^{-1} K^{-1}	-
Air temperature : T_a	20 °C	-
Air thermal expansion coef. : β_a	3.69×10^{-3} K^{-1}	-
Initial lava flow temperature : T_{ini}	800 °C	-
Initial substratum temperature : T_{sub}	20 °C	-
Lava flow emissivity : ε	0.925	(Salisbury and D'Aria, 1994)
Reference lava density at T_{ref} : ρ_{ref}	2630 kg m^{-3}	(Luhr, 2002)
Reference temperature: T_{ref}	20°C	(Luhr, 2002)
Simulation start date	01/01/2015	-
Thermal expansion coefficient : β	1×10^{-5} K^{-1} or 3.5×10^{-5} K^{-1}	(Bauer and Handin, 1983; Mallela et al., 2005; Murase and McBirney, 1973)
Numerical parameters		
Polynomial degree of elements	1	-
Number of elements into the flow	100	-
Number of elements into the substratum	200	-
Stability coefficient	0.01	-

Table 4: List of parameters used for the numerical modeling of the lava flow thermal compaction and associated references.

4. Discussion

4.1 The 2014-2015 effusive activity of Volcàn de Colima

Using the DEM difference (Fig. 4A) together with the temporal constrain provided by coherence evolution, we identified at least 3 massive lava flows emplaced between November 2014 and July 2015. Two of them (W and S–W) results from the overflow of the dome near the end of 2014. The third one (S) occurred after the July 2015 explosion. Each lava flow is thick and presents sharp edges, which suggests here the small influence of spreading and breakout effects as sometimes described in the literature (Tuffen et al., 2013). Both S–W and S lava flows show an increased in their thickness close to their front (Fig 4A). This increases might be associated with the sharp decrease of the topographic slope (from ~25° to 15°~, Fig. 4B). On the contrary, the W lava flow does not present the same increased in its thickness near its front, probably related to the absence of significant slope change along the lava flow.

The extruding rate we estimate around 1-2 $m^3 s^{-1}$ between November 2014 and February 2015 is 100 to 1000 times higher than the extruding rates derived in 2010–2011 from the seismic signature of rockfalls (Mueller et al., 2013), and 15 to 30 times larger than published estimations for the long term extrusion rate (Luhr and Carmichael, 1980; Luhr and Prestegaard, 1988). It highlights the temporal variations in the extrusion rate as already previously evidenced (Mueller et al., 2013). This larger value might also evidence an increase in the volcano activity preceding the large July 2015 eruptive event.

4.2. Use of physical *a priori* to retrieve the 3D displacement field from InSAR measurements:

Most InSAR studies dealing with lava flows deformation consider the LOS displacement as the projection of a vertical motion along the LOS using the following equation (e.g. Wittmann et al., 2017):

$$d_V = -\frac{d_{LOS}}{cos(\theta)} \qquad (9)$$

In order to test the validity of this assumption, we computed the vertical displacement rate using Eq. 9 for both ascending and descending tracks. As the horizontal viewing angle, on the descending track, is almost perpendicular to the direction of the flow, the results obtained are similar to the ones derived with our approach based on the physical *a priori* that the horizontal displacement is directed along the maximum slope. This is clearly not the case on the ascending track for which the horizontal motion cannot be neglected except at the end of the studied period (Fig. 8C). However, after December 2015, horizontal motion becomes negligible and LOS displacements for both tracks can be used alone to correctly estimate vertical displacements. To summarize, Eq. 9 can only be applied when the LOS is perpendicular to the flow direction (that is to say the horizontal projection of the satellite pathway is parallel to the flow direction), or when horizontal motion is negligible.

The method we propose to reconstruct the 3D displacement field has the advantage of relying on a physical *a priori*. We assume that the horizontal motion over the lava flow is directed along the maximum slope direction. The use of this *a priori* is not necessary when several geometries of acquisition from different satellites are available (Wright et al., 2004, Peltier et al., 2017). As in most studies, in our case only two tracks from the same satellite, the ascending and descending ones, are available, but contrary to what is commonly done (e.g. Samsonov et al., 2017) we do not consider the north-south displacement as null. Instead, we consider that the direction of the horizontal motion is mainly controlled by the local topography. This method can also be applied to studies dealing with other types of deformation sources observed on volcanoes, such as reservoir pressurization or dike propagation. The displacements associated with such sources are usually well predicted by simple analytical models provided the sources are deep enough to preclude any strong influence of the topography (e.g. Mogi, 1958 and Okada, 1985). By defining a given central pressurization point or a given dislocation line, it is possible to predict the direction of the expected horizontal displacement. Thus, our approach could potentially be used to reconstruct the 3D deformation field on volcanoes, by introducing an *a priori* with respect to the horizontal displacement direction, for both ascending and descending tracks of the same satellite.

4.3. Origin of deformation: magma downward flow contribution in addition to thermal compaction and loading.

The vertical and horizontal displacements measured in Fig. 7–8 have different causes related to the deposit of a new lava flow: substratum deformation induced by a loading effect (viscoelastic and poroelastic relaxations), thermal contractions, and possibly displacements resulting from the ongoing flow, or shearing, of the lava on the flank (Fig. 11A). The two latter effects are limited to the lava flow itself, whereas the loading effect extends beyond the lava flow contour line. In the following section, we investigate the various potential causes of the observed displacements in order to discriminate the relative importance of each effect.

When a flow is emplaced, it produces ground loading and induces viscoelastic and/or poroelastic relaxation of the substratum and associated displacement in the vertical direction (Briole et al., 1997; Lu et al., 2005). Poroelastic displacement can reach several centimeters but only during the few days following lava flow emplacement (Lu et al., 2005). As the InSAR time series starts a few months after the emplacement, poroelastic effects on the displacement rate should be minimal. The viscous relaxation of the substratum is a slower process, and is expected to be the main cause of the vertical subsidence observed around the flow (Fig. 7). Viscoelastic deformation can be inferred from the load, which is directly proportional to the lava thickness, although the estimate is strongly dependent on the substratum rheology profile. Two end members are generally considered. The first end-member considers the substratum as an upper finite viscoelastic layer of given thickness lying on a rigid material. The loading stress is then assumed as constant within the upper layer (Briole et al., 1997). The second end-member considers an infinite elastic half space, where the loading stress decreases with depth (Watanabe et al., 2002). The amount and temporal evolution of viscoelastic displacement is strongly affected by these assumptions. For example, after 1 year with the same load and with the same substratum mechanical properties, the first assumption yields a displacement in the order of centimeters, whereas the second one predicts deformation of the order of millimeters. A good knowledge of the substratum structure and mechanical properties is required in order to make a reliable estimate of the viscoelastic deformation.

The displacement field induced by thermal compaction has been modeled in section 3.4. Its amplitude is dependent on the poorly constrained thermal expansion coefficient but the modeling results can be used to discuss the relative influence of this process. Figure 10B displays the residuals obtained by removing our modeled thermo-elastic displacement from the observed displacement rate (red and blue curves on Fig. 10B). The residual horizontal motion can mostly be attributed to flow motion or lava flow shearing, depending on the amount of friction at the lava flow/substratum interface. This is confirmed by the fact that horizontal displacements recorded around the lava flow are very weak, indicating negligible horizontal motion of the substratum. As sliding motion also produces vertical displacement, we estimated and corrected the vertical displacement for this effect considering the volcano slope (see solid and dashed black lines in Fig. 10B). With the largest thermal expansion coefficient ($\beta=3.5 \times 10^{-5}$ K^{-1}), the residual vertical displacement is mostly explained by flow motion. That would imply negligible viscoelastic deformation and would be in contradiction with the displacement recorded on the substratum around the flow. Thus, the thermal contraction coefficient must be lower than $\beta=3.5 \times 10^{-5}$ K^{-1}. This is also supported by laboratory observations showing that the thermal expansion coefficient decreased with the presence of cracks (Richter and Simmons, 1974). Analysis of samples coming from the dome at Volcàn de Colima shows that a decrease in temperature, or an increase in the strain rate, promotes the formation of cracks (Lavallée et al., 2012). The better agreement of the results with a low thermal expansion tends to indicate the presence of cracks and fractures within the emplaced material. With the lowest thermal expansion coefficient ($\beta=1 \times 10^{-5}$ K^{-1}), the amplitude of the displacement induced by thermal contraction is smaller. It follows that residual displacements are larger on the vertical component (where thermal compaction induces a downward displacement) and smaller on the horizontal one (where thermal compaction induces an uphill displacement). Using a thermal expansion coefficient $\beta=1 \times 10^{-5}$ K^{-1}, the residual vertical displacement corrected for magma flow effects decreases from 100.7 mm yr^{-1} to 79.4 mm yr^{-1} (plain black curve in Fig. 10B), which is much more consistent with the average vertical displacements recorded around the lava flow (Fig. 7). This residual value is expected to result from the viscoelastic compaction alone, acting not only on the lava flow itself but also around it. Based on these estimates, the viscoelastic compaction, the thermal contraction and the effect of downward lava flow would account for about 50%, 25% and 25%, respectively, of the observed vertical displacement 8 months after the magma flow emplacement (Fig. 11B). The amount of horizontal displacement produced by lava downward flow (solid red curve on Fig. 10B) seems to decrease relatively rapidly with time and tends towards zero at the end of the studied period. At this time, 75% of the observed displacement can be explained by viscoelastic compaction, and 25% by thermal contraction of the lava (Fig. 11B).

Lava flow motion had been evidenced several months after emplacement for rhyolitic obsidian flow at Cordon Caulle volcano, Chile by field observations (Tuffen et al., 2013) but to our knowledge such a downward flow displacement has never been isolated from InSAR measurements before. The fact that it can be observed 8 months after the flow emplacement is probably related to the high viscosity of this andesitic lava flow and the steepness of the slope on the edifice flanks, two uncommon characteristics with regard to previous studies (see Table 1). This horizontal displacement can be used to calculate a rough estimate of the lava bulk viscosity η. By considering that horizontal displacements result from the shearing of the lava flow (i.e. no slip at the lava/substratum interface) characterized by a Newtonian rheology, the viscosity can be estimated with:

$$\eta = \frac{\rho\, g\, H^2 \sin\alpha \cos\alpha}{2\, v_h}, \qquad (10)$$

where ρ = 2600 kg m^{-3}, the lava bulk density, g, the gravitational acceleration, H = 40.6m, the lava flow thickness, α = 20.9°, the volcano slope, and v_h, the horizontal surface displacement. Equation 19 estimates the lava flow bulk viscosity at around 10^{15} Pa s in August 2015, at the beginning of the studied period, and reaching a value of 10^{17} Pa s at the end of this period. The assumption of a Newtonian behavior is not really expected to be verified for a highly crystalized lava (Lavallée et al., 2007) and the temporal evolution of the viscosity we derived cannot be explained by an Arrhenius law given the modeled variation in temperature. However, our estimations both in terms of order of magnitude and temporal evolution are in relative good agreement with the prediction from a general non-Arrhenius law for lava dome materials. In particular, our estimations are consistent with the law linking the apparent viscosity of the emplaced material and the shear rate derived by Lavallée et al., (2007) for moderate strain rates (larger than the ones we measure) on dome material from Colima Volcano.

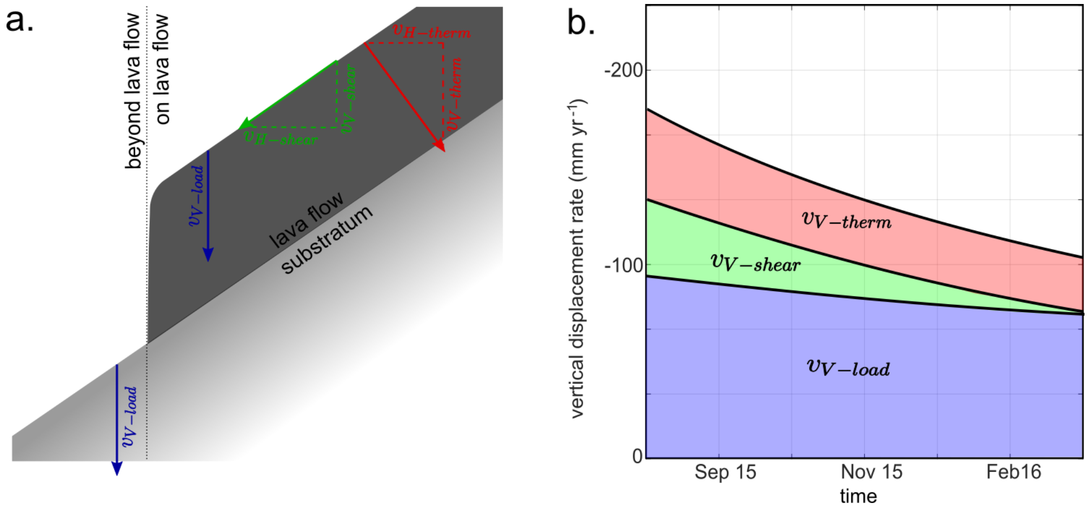

Figure 11: Causes of the observed displacement **[A]** Sources of deformations on and outside the lava flow area. The darker zone represents the lava flow emplaced on an inclined substratum. The blue arrows correspond to the vertical viscoelastic displacement imposed by the load (this displacement is induced both on and around the lava flow area). The red and green arrows are for the thermal contraction and lava downward motion, respectively (these contributions are both restricted to the lava flow area). Both can be decomposed into horizontal and vertical components. **[B]** Evolution of the different increments of the lava flow deformations. The color code is the same as the arrows on Fig. 11A.

5. Conclusion

InSAR measurements here reveal significant lava flow motions on andesitic lava flow emplaced on steep slopes up to 10 months after lava supply stops. In more details, this study highlights the difficulties in using remote sensing datasets to study volcanic activity on andesitic stratovolcanoes. Low coherence due to steep flanks, vegetation cover and frequent ash deposits prevents the use of decorrelation to map lava flows precisely. To overcome these problems, mapping can be performed using DEMs, with the additional advantage of being able to quantify the volume of lava emplaced and to derive the associated eruption rate. At Volcàn de Colima, we estimated a mean extrusion rate of around 1–2 m^3 s^{-1} over a 4 month period (November 2014 to February 2015). In order to maximize on the coherence, we use an alternative approach to the classical one used on shield volcanoes, which is based on averaging the difference between coherence maps characterized by similar spatio-temporal baselines in order to highlight the timing of new deposits. We also propose an approach to reconstruct the 3D displacement field of lava flows, from 2 viewing angles, using a physical assumption on the horizontal motion direction, here considered to be controlled by the local topography. The 3D displacement field retrieved at Volcán de Colima from InSAR time series inversions shows that horizontal displacements are still significant on the SW lava flow a few months after lava emplacement despite its apparent inactivity. Such behavior might be common on highly viscous lava flows emplaced on steep slopes. Analysis of the observed displacements through numerical modeling of the thermal compaction indicates that thermal contraction, viscoelastic loading, and flow motion all play a significant role in the measured displacement field and brings quantitative constrains on both the effective lava viscosity and its thermal expansion coefficient.

Acknowledgement:

This study was supported by CNES through the TOSCA project MerapiSAR. Pleiades images were available through an ISIS project. SAR images were provided by ESA and downloaded from the CNES operating platform at https://peps.cnes.fr/rocket/#/home. TanDEM-X DEM was provided by the German Space Agency through proposal DEM_GEOL1315 (©DLR 2015). This manuscript benefited greatly from the constructive reviews and comments of two anonymous reviewers. Authors declare no conflict of interest.

References:

Amelung, F., Day, S., 2002. InSAR observations of the 1995 Fogo, Cape Verde, eruption: Implications for the effects of collapse events upon island volcanoes. Geophys. Res. Lett. 29, 47-1-47–4.

Arnold, D.W.D., Biggs, J., Anderson, K., Vallejo Vargas, S., Wadge, G., Ebmeier, S.K., Naranjo, M.F., Mothes, P., 2017. Decaying Lava Extrusion Rate at El Reventador Volcano, Ecuador, Measured Using High-Resolution Satellite Radar. J. Geophys. Res. Solid Earth.

Bato, M.G., Froger, J.L., Harris, A.J.L., Villeneuve, N., 2016. Monitoring an effusive eruption at Piton de la Fournaise using radar and thermal infrared remote sensing data: insights into the October 2010 eruption and its lava flows. Geol. Soc. Lond. Spec. Publ. 426, 533–552. https://doi.org/10.1144/SP426.30

Bauer, S.J., Handin, J., 1983. Thermal expansion and cracking of three confined water-saturated igneous rocks to 800°C. Rock Mech. Rock Eng. 16, 181–198. https://doi.org/10.1007/BF01033279

Briole, P., Massonnet, D., Delacourt, C., 1997. Post-eruptive deformation associated with the 1986–87 and 1989 lava flows of Etna detected by radar interferometry. Geophys. Res. Lett. 24, 37–40. https://doi.org/10.1029/96GL03705

Broxton, M.J., Edwards, L.J., 2008. The Ames Stereo Pipeline: Automated 3D surface reconstruction from orbital imagery, in: Lunar and Planetary Science Conference. p. 2419.

Capra, L., Macías, J.L., Cortés, A., Dávila, N., Saucedo, R., Osorio-Ocampo, S., Arce, J.L., Gavilanes-Ruiz, J.C., Corona-Chávez, P., García-Sánchez, L., Sosa-Ceballos, G., Vázquez, R., 2016. Preliminary report on the July 10–11, 2015 eruption at Volcán de Colima: Pyroclastic density currents with exceptional runouts and volume. J. Volcanol. Geotherm. Res. 310, 39–49. https://doi.org/10.1016/j.jvolgeores.2015.11.022

Cassidy, M., Cole, Paul.D., Hicks, K.E., Varley, N.R., Peters, N., Lerner, A.H., 2015. Rapid and slow: Varying magma ascent rates as a mechanism for Vulcanian explosions. Earth Planet. Sci. Lett. 420, 73–84. https://doi.org/10.1016/j.epsl.2015.03.025

Chaussard, E., 2016. Subsidence in the Parícutin lava field: Causes and implications for interpretation of deformation fields at volcanoes. J. Volcanol. Geotherm. Res. 320, 1–11. https://doi.org/10.1016/j.jvolgeores.2016.04.009

Chen, Y., Zhang, K., Tan, K., Feng, X., Li, H., 2018. Long-Term Subsidence in Lava Fields at Piton de la Fournaise Volcano Measured by InSAR: New Insights for Interpretation of the Eastern Flank Motion. Remote Sens. 10, 597.

Dietterich, H.R., Poland, M.P., Schmidt, D.A., Cashman, K.V., Sherrod, D.R., Espinosa, A.T., 2012. Tracking lava flow emplacement on the east rift zone of Kīlauea, Hawaiʻi, with synthetic aperture radar coherence. Geochem. Geophys. Geosystems 13, Q05001. https://doi.org/10.1029/2011GC004016

Doin, M.-P., Lasserre, C., Peltzer, G., Cavalié, O., Doubre, C., 2009. Corrections of stratified tropospheric delays in SAR interferometry: Validation with global atmospheric models. J. Appl. Geophys., Advances in SAR Interferometry from the 2007 Fringe Workshop 69, 35–50. https://doi.org/10.1016/j.jappgeo.2009.03.010

Doin, M.-P., Lodge, F., Guillaso, S., Jolivet, R., Lasserre, C., Ducret, G., Grandin, R., Pathier, E., Pinel, V., 2012. Presentation Of The Small Baseline NSBAS Processing Chain On A Case Example: The ETNA Deformation Monitoring From 2003 to 2010 Using ENVISAT Data. Presented at the Fringe 2011, p. 98.

Ebmeier, S.K., Biggs, J., Mather, T.A., Elliott, J.R., Wadge, G., Amelung, F., 2012. Measuring large topographic change with InSAR: Lava thicknesses, extrusion rate and subsidence rate at Santiaguito volcano, Guatemala. Earth Planet. Sci. Lett. 335–336, 216–225. https://doi.org/10.1016/j.epsl.2012.04.027

Felpeto, A., Araña, V., Ortiz, R., Astiz, M., García, A., 2001. Assessment and Modelling of Lava Flow Hazard on Lanzarote (Canary Islands). Nat. Hazards 23, 247–257. https://doi.org/10.1023/A:1011112330766

Fournier, T.J., Pritchard, M.E., Riddick, S.N., 2010. Duration, magnitude, and frequency of subaerial volcano deformation events: New results from Latin America using InSAR and a global synthesis. Geochem. Geophys. Geosystems 11.

Gaddis, L.R., 1992. Lava-flow characterization at Pisgah volcanic field, California, with multiparameter imaging radar. GSA Bull. 104, 695–703. https://doi.org/10.1130/0016-7606(1992)104<0695:LFCAPV>2.3.CO;2

Grandin, R., 2015. Interferometric Processing of SLC Sentinel-1 TOPS Data. Presented at the FRINGE 2015, p. 36.

Lavallée, Y., Hess, K.-U., Cordonnier, B., Dingwell, D.B., 2007. Non-Newtonian rheological law for highly crystalline dome lavas. Geology 35, 843–846. https://doi.org/10.1130/G23594A.1

Lavallée, Y., Varley, N., Alatorre-Ibargüengoitia, M., Hess, K.-U., Kueppers, U., Mueller, S., Richard, D., Scheu, B., Spieler, O., Dingwell, D., 2012. Magmatic architecture of dome-building eruptions at Volcán de Colima, Mexico. Bull. Volcanol. 74, 249–260.

Lee, H., Liu, J.G., 2001. Analysis of topographic decorrelation in SAR interferometry using ratio coherence imagery. IEEE Trans. Geosci. Remote Sens. 39, 223–232. https://doi.org/10.1109/36.905230

Lesage, P., Carrara, A., Pinel, V., Arámbula-Mendoza, R., 2018. Absence of Detectable Precursory Deformation and Velocity Variation Before the Large Dome Collapse of July 2015 at Volcán de Colima, Mexico. Front. Earth Sci. 6. https://doi.org/10.3389/feart.2018.00093

Lu, Z., Masterlark, T., Dzurisin, D., 2005. Interferometric synthetic aperture radar study of Okmok volcano, Alaska, 1992–2003: Magma supply dynamics and postemplacement lava flow deformation. J. Geophys. Res. Solid Earth 110, B02403. https://doi.org/10.1029/2004JB003148

Luhr, J.F., 2002. Petrology and geochemistry of the 1991 and 1998–1999 lava flows from Volcán de Colima, México: implications for the end of the current eruptive cycle. J. Volcanol. Geotherm. Res. 117, 169–194. https://doi.org/10.1016/S0377-0273(02)00243-3

Luhr, J.F., Carmichael, I.S.E., 1990. Petrological monitoring of cyclical eruptive activity at Volcán Colima, Mexico. J. Volcanol. Geotherm. Res. 42, 235–260. https://doi.org/10.1016/0377-0273(90)90002-W

Luhr, J.F., Carmichael, I.S.E., 1980. The Colima Volcanic complex, Mexico. Contrib. Mineral. Petrol. 71, 343–372. https://doi.org/10.1007/BF00374707

Luhr, J.F., Prestegaard, K.L., 1988. Caldera formation at Volcán Colima, Mexico, by a large large holocene volcanic debris avalanche. J. Volcanol. Geotherm. Res. 35, 335–348. https://doi.org/10.1016/0377-0273(88)90027-3

Macorps, E., Charbonnier, S.J., Varley, N.R., Capra, L., Atlas, Z., Cabré, J., 2017. Stratigraphy, sedimentology and inferred flow dynamics from the July 2015 block-and-ash flow deposits at Volcán de Colima, Mexico. J. Volcanol. Geotherm. Res. https://doi.org/10.1016/j.jvolgeores.2017.09.025

Mallela, J., Abbas, A., Harman, T., Rao, C., Liu, R., Darter, M., 2005. Measurement and Significance of the Coefficient of Thermal Expansion of Concrete in Rigid Pavement Design. Transp. Res. Rec. J. Transp. Res. Board 1919, 38–46. https://doi.org/10.3141/1919-05

Mogi, K., 1958. Relations between the Eruptions of Various Volcanoes and the Deformations of the Ground Surfaces around them. Earthq. Res. Inst. 36, 99–134.

Mossoux, S., Saey, M., Bartolini, S., Poppe, S., Canters, F., Kervyn, M., 2016. Q-LAVHA: A flexible GIS plugin to simulate lava flows. Comput. Geosci. 97, 98–109. https://doi.org/10.1016/j.cageo.2016.09.003

Mueller, S.B., Varley, N.R., Kueppers, U., Lesage, P., Reyes Davila, G.Á., Dingwell, D.B., 2013. Quantification of magma ascent rate through rockfall monitoring at the growing/collapsing lava dome of Volcán de Colima, Mexico. Solid Earth 4, 201–213. https://doi.org/10.5194/se-4-201-2013

Murase, T., McBirney, A.R., 1973. Properties of Some Common Igneous Rocks and Their Melts at High Temperatures. GSA Bull. 84, 3563–3592. https://doi.org/10.1130/0016-7606(1973)84<3563:POSCIR>2.0.CO;2

Okada, Y., 1985. Surface deformation due to shear and tensile faults in a half-space. Bull. Seismol. Soc. Am. 75, 1135–1154.

Patrick, M.R., Dehn, J., Dean, K., 2004. Numerical modeling of lava flow cooling applied to the 1997 Okmok eruption: Approach and analysis. J. Geophys. Res. Solid Earth 109, B03202. https://doi.org/10.1029/2003JB002537

Peltier, A., Froger, J.-L., Villeneuve, N., Catry, T., 2017. Assessing the reliability and consistency of InSAR and GNSS data for retrieving 3D-displacement rapid changes, the example of the 2015 Piton de la Fournaise eruptions. J. Volcanol. Geotherm. Res. 344, 106–120.

Pinel, V., Hooper, A., De la Cruz-Reyna, S., Reyes-Davila, G., Doin, M.P., Bascou, P., 2011. The challenging retrieval of the displacement field from InSAR data for andesitic stratovolcanoes : case study of Popocatepetl and Colima Volcano, Mexico. J. Volcanol. Geotherm. Res. 200, 49–61. https://doi.org/10.1016/j.jvolgeores.2010.12.002

Pinel, V., Poland, M.P., Hooper, A., 2014. Volcanology: Lessons learned from Synthetic Aperture Radar imagery. J. Volcanol. Geotherm. Res. 289, 81–113. https://doi.org/10.1016/j.jvolgeores.2014.10.010

Poland, M.P., 2014. Time-averaged discharge rate of subaerial lava at Kīlauea Volcano, Hawaiʻi, measured from TanDEM-X interferometry: Implications for magma supply and storage during 2011–2013. J. Geophys. Res. Solid Earth 119, 2014JB011132. https://doi.org/10.1002/2014JB011132

Rabus, B.T., Fatland, D.R., 2000. Comparison of SAR-interferometric and surveyed velocities on a mountain glacier: Black Rapids Glacier, Alaska, U.S.A. J. Glaciol. 46, 119–128. https://doi.org/10.3189/172756500781833214

Reyes-Dávila, G.A., Arámbula-Mendoza, R., Espinasa-Pereña, R., Pankhurst, M.J., Navarro-Ochoa, C., Savov, I., Vargas-Bracamontes, D.M., Cortés-Cortés, A., Gutiérrez-Martínez, C., Valdés-González, C., Domínguez-Reyes, T., González-Amezcua, M., Martínez-Fierros, A., Ramírez-Vázquez, C.A., Cárdenas-González, L., Castañeda-Bastida, E., Vázquez Espinoza de los Monteros, D.M., Nieto-Torres, A., Campion, R., Courtois, L., Lee, P.D., 2016. Volcán de Colima dome collapse of July, 2015 and associated pyroclastic density currents. J. Volcanol. Geotherm. Res. 320, 100–106. https://doi.org/10.1016/j.jvolgeores.2016.04.015

Richter, D., Simmons, G., 1974. Thermal expansion behavior of igneous rocks. Int. J. Rock Mech. Min. Sci. Geomech. Abstr. 11, 403–411. https://doi.org/10.1016/0148-9062(74)91111-5

Robin, C., Mossand, P., Camus, G., Cantagrel, J.-M., Gourgaud, A., Vincent, P.M., 1987. Eruptive history of the Colima volcanic complex (Mexico). J. Volcanol. Geotherm. Res. 31, 99–113. https://doi.org/10.1016/0377-0273(87)90008-4

Rowland, S.K., Harris, A.J.L., Wooster, M.J., Amelung, F., Garbeil, H., Wilson, L., Mouginis-Mark, P.J., 2003. Volumetric characteristics of lava flows from interferometric radar and multispectral satellite data: the 1995 Fernandina and 1998 Cerro Azul eruptions in the western Galápagos. Bull. Volcanol. 65, 311–330. https://doi.org/10.1007/s00445-002-0262-x

Salisbury, J.W., D'Aria, D.M., 1994. Emissivity of terrestrial materials in the 3–5 µm atmospheric window. Remote Sens. Environ. 47, 345–361. https://doi.org/10.1016/0034-4257(94)90102-3

Samsonov, S., d'Oreye, N., 2012. Multidimensional time-series analysis of ground deformation from multiple InSAR data sets applied to Virunga Volcanic Province. Geophys. J. Int. 191, 1095–1108.

Samsonov, S.V., Feng, W., Peltier, A., Geirsson, H., d'Oreye, N., Tiampo, K.F., 2017. Multidimensional Small Baseline Subset (MSBAS) for volcano monitoring in two dimensions: Opportunities and challenges. Case study Piton de la Fournaise volcano. J. Volcanol. Geotherm. Res. 344, 121–138.

Savov, I.P., Luhr, J.F., Navarro-Ochoa, C., 2008. Petrology and geochemistry of lava and ash erupted from Volcán Colima, Mexico, during 1998–2005. J. Volcanol. Geotherm. Res. 174, 241–256. https://doi.org/10.1016/j.jvolgeores.2008.02.007

Schaber, G.G., Elachi, C., Farr, T.G., 1980. Remote sensing data of SP Mountain and SP lava flow in north-central Arizona. Remote Sens. Environ. 9, 149–170.

Schaefer, L., Lu, Z., Oommen, T., 2016. Post-eruption deformation processes measured using ALOS-1 and UAVSAR InSAR at Pacaya Volcano, Guatemala. Remote Sens. 8, 73.

Sennert, S.K.(ed.)., 2015a. Global Volcanism Program, 2015. Report on Colima (Mexico). 18 February-24 February 2015. Smithson. Inst. US Geol. Surv.

Sennert, S.K.(ed.)., 2015b. Global Volcanism Program, 2015. Report on Colima (Mexico) 15 July-21 July 2015. Smithson. Inst. US Geol. Surv.

Sigmundsson, F., Vadon, H., Massonnet, D., 1997. Readjustment of the Krafla spreading segment to crustal rifting measured by satellite radar interferometry. Geophys. Res. Lett. 24, 1843–1846.

Stevens, N.F., Wadge, G., Murray, J.B., 1999. Lava flow volume and morphology from digitised contour maps: a case study at Mount Etna, Sicily. Geomorphology 28, 251–261.

Stevens, N.F., Wadge, G., Williams, C.A., Morley, J.G., Muller, J.-P., Murray, J.B., Upton, M., 2001. Surface movements of emplaced lava flows measured by synthetic aperture radar interferometry. J. Geophys. Res. Solid Earth 106, 11293–11313. https://doi.org/10.1029/2000JB900425

Terunuma, T., Nishida, K., Amada, T., Mizuyama, T., Sato, I., Urai, M., 2005. Detection of traces of pyroclastic flows and lahars with satellite synthetic aperture radars. Int. J. Remote Sens. 26, 1927–1942. https://doi.org/10.1080/01431160512331326576

Tuffen, H., James, M.R., Castro, J.M., Schipper, C.I., 2013. Exceptional mobility of an advancing rhyolitic obsidian flow at Cordón Caulle volcano in Chile. Nat. Commun. 4, 2709. https://doi.org/10.1038/ncomms3709

Voight, B., Constantine, E.K., Siswowidjoyo, S., Torley, R., 2000. Historical eruptions of Merapi Volcano, Central Java, Indonesia, 1768–1998. J. Volcanol. Geotherm. Res. 100, 69–138. https://doi.org/10.1016/S0377-0273(00)00134-7

Watanabe, T., Masuyama, T., Nagaoka, K., Tahara, T., 2002. Analog experiments on magma-filled cracks. Earth Planets Space 54, 1247–1261. https://doi.org/10.1186/BF03352453

Wittmann, W., Sigmundsson, F., Dumont, S., Lavallée, Y., 2017. Post-emplacement cooling and contraction of lava flows: InSAR observations and a thermal model for lava fields at Hekla volcano, Iceland. J. Geophys. Res. Solid Earth 122, 2016JB013444. https://doi.org/10.1002/2016JB013444

Wright, T.J., Parsons, B.E., Lu, Z., 2004. Toward mapping surface deformation in three dimensions using InSAR. Geophys. Res. Lett. 31.

Zan, F.D., Guarnieri, A.M., 2006. TOPSAR: Terrain Observation by Progressive Scans. IEEE Trans. Geosci. Remote Sens. 9, 2352–2360. https://doi.org/10.1109/TGRS.2006.873853

Zebker, H.A., Rosen, P., Hensley, S., Mouginis-Mark, P.J., 1996. Analysis of active lava flows on Kilauea volcano, Hawaii, using SIR-C radar correlation measurements. Geology 24, 495–498. https://doi.org/10.1130/0091-7613(1996)024<0495:AOALFO>2.3.CO;2

Zebker, H.A., van Zyl, J.J., Held, D.N., 1987. Imaging radar polarimetry from wave synthesis. J. Geophys. Res. Solid Earth 92, 683–701. https://doi.org/10.1029/JB092iB01p00683

Zebker, H.A., Villasensor, J., 1992. Decorrelation in interferometric radar echoes. IEEE Trans. Geosci. Remote Sens. 30, 950–959. https://doi.org/10.1109/36.175330

Supplementary information A:

This supplementary information details the implementation of the lava flow thermal contraction model using a Finite Element Method.

A1. FEM cooling model

The cooling model used a classic FEM implementation. We present here the key points of the implementation used. For a more complete presentation about the numerical method, see Zienkiewicz et al., (2000). Assuming no additional heat source, the diffusion of heat, by conduction, is given by the heat equation and associated boundary conditions. Mathematically, it yields, in 1D:

$$\frac{\partial T(x,t)}{\partial t} + \frac{k(T)}{\rho(T)Cp(T)} \frac{\partial^2 T(x,t)}{\partial x^2} = 0 \,, \tag{A1A}$$

$$\frac{\partial\, T}{\partial\, t}\,(H,t) = \frac{Q_{tot}(t)}{C_p(t)}, \tag{A1B}$$

$$\frac{\partial\, T}{\partial\, x}(h,t) = 0. \tag{A1C}$$

Equation A1A corresponds to the heat diffusion equation, with $T(x,t)$ the temperature at location x and time$t$. The heat diffusion coefficient is presented here as the ratio of the thermal conductivity, $k(T)$, over the product of the material density $\rho(T)$ and heat capacity $Cp(T)$. Given that these parameters depend on the local temperature, they vary in space and must be included in the first spatial derivative in Eq. A1A. As the temperature evolution of k, ρ, and Cp are relatively weak, their spatial derivatives can be neglected and we can remove them from the first spatial derivative in Eq. A1A. Equation A1B is the boundary condition at the top of the lava flow. The surface temperature evolution depends on the total heat flux, Q_{tot} (radiation and natural convection) going from the lava flow surface to the air. The index H is the lava flow thickness and expresses the coordinates of the lava flow top surface. Equation A1C represents the boundary condition at the bottom part of the model where the heat flux is considered null. The index h corresponds to the considered thickness of the substratum and refers to the coordinate of the bottom part of the physical model.

After transforming Eq. A1 into its weak form, the solution for each element is computed with respect to reference element [-1,1] using polynomials of degree 1. Linear mapping is used to map each element to the reference one: $F_e(\xi) = \gamma\xi + \lambda = x$, where ξ and x represent the spatial coordinate in the reference element and in the physical domain, respectively. The coefficients γ and λ, depend on the element's position and length, and are defined as $\gamma = (b_e - a_e)/2$ and $\lambda = (a_e + b_e)/2$, with a_e and b_e corresponding to the left and right edge positions of a given element, e, respectively. The change of variable between ξ and x implies the use of the Jacobian, J_e, defined as $J_e = \delta x/\delta\xi$.

For the reference element, the solution is computed using a Lagrange polynomial interpolation. For the first term in the left hand side of Eq. A1 involving the temporal derivative of the temperature, the so-called local mass matrix, M_{ij}, associated to the element e is given by:

$$M_{ij}(e) = \sum_{l=1}^{L_e} h_i(\xi_l)h_j(\xi_l)w_l J_e d\xi, \qquad \text{(A.2)}$$

where l is the integration point index, and L , the number of integration points within the reference element. w_l is the l$^{\text{th}}$ integration weight and the variables h are the values of the Lagrange polynomials, linked to the integration points on the reference element (indices i and j

going from 1 to L_e). The discretization of the second term on the left hand side of Eq. A1, involving the Laplace operator of the temperature field yields the local stiffness matrix, K_{ij}, which is computed as:

$$K_{ij}(e) = \sum_{l=1}^{L_e} h_i'(\xi_l) h_j'(\xi_l) w_l \frac{1}{J_e} d\xi, \tag{A.3}$$

Where $h_i'(\xi_l)$ stands for the value of the spatial derivative of the ith Lagrange polynomial at the lth integration point. The local mass and stiffness matrices associated with each element are assembled and become M and K, the global mass and stiffness matrices, respectively. The assembly process is implemented through the use of the so-called connectivity matrix, Q, and its transpose, Q^T(Deville et al., 2002, p. 193). Thus, Eq. A1 become:

$$Q^T M Q \frac{\partial}{\partial t} U + Q^T K Q U = 0, \tag{A.4}$$

where U represents the continuous vector whose indices are the temperature values $T(x,t)$ at the finite element nodes.

The time evolution of temperature is computed with a first order forward finite-difference scheme:

$$U(t+1) = U(t) - \Delta t (Q^T M Q)^{-1} Q^T K Q U(t) \tag{A.5}$$

With Δt the time step imposed on the model. To ensure the stability of the model, the stability criterion must be satisfied (Recktenwald, 2004):

$$\Delta t = p \frac{\Delta x^2 \rho C p}{k}, \tag{A.6}$$

with the stability coefficient, p<0.5, and, Δx, the lowest distance between two finite element nodes in the physical domain.

A2. Implementation of boundary conditions

At the bottom of the substratum, a Neumann boundary condition is imposed, meaning that there is no heat flux ($\partial T / \partial x = 0$). At the lava flow surface, we used a Dirichlet boundary condition by imposing a temperature, at each time step. Carrying out the Neumann boundary condition in the finite element model is natural and does not require special treatment. On the contrary, the Dirichlet boundary condition has to be enforced at each time step, with the desired temperature being input. This temperature is initially fixed at that of the lava flow, and then decreases with time due to radiative and convective heat loss to the air. The natural convective and radiative heat fluxes at the surface of the lava flow are computed as in Patrick et al., (2004). The surface temperature is then computed using a first order finite difference scheme, function of the total surface heat flux, Q_{tot} as:

$$T_{surf}(t + \Delta t) = T_{surf} + \Delta t \frac{Q_{tot}}{C_p}. \quad \text{(A.7)}$$

At the initiation of the simulation, as the surface temperature decreases rapidly, the time step required to correctly sample the variations of the Dirichlet boundary condition at the top of the lava flow using Eq. A7 is smaller than for Eq. A5. Thus, we limit the time step to have, at maximum, a change of surface temperature of 1% for each iteration, before updating the total heat flux. Thus, time steps increase at the beginning of the simulation, with the decrease of the surface temperature, before reaching the time step imposed by Eq A6.

A3. Thermal compaction approach

The thermal contraction or expansion of elements are computed, at each time step, after a new temperature field has been computed. The length evolution of an element depends on its temperature change. As the elements are sampled by several nodes, an average of the temperature, $\acute{T}_e$, is needed and computed as:

$$\acute{T}_e = \sum_l^{L_e} T(l,t) w_l. \tag{A.8}$$

The length evolution of each element, dh_e, is computed as a function of the temporal evolution of the element's average temperature with:

$$\frac{d\,h_e}{d\,t} = \beta\,\frac{1+\nu}{1-\nu}\,\frac{\partial\,T}{\partial\,t}, \tag{A.9}$$

with h_e, the element length, β, the thermal expansion coefficient and ν, the Poisson coefficient. Eq. (A.9) is discretized using a first order finite difference scheme in time, and yields:

$$dh_e(t) = h_e(t-\Delta t)\beta\frac{1+\nu}{1-\nu}\left(\acute{T}_e(t) - \acute{T}_e(t-\Delta t)\right), \tag{A.10}$$

With h_e the element length and $\acute{T}_e$ its average temperature. After computing the new elements length and integration point positions, the cooling model is adjusted by updating J_e, F_e, M and K. The elements' densities, heat capacities and thermal conductivities are also updated, at each time step, with their new average temperature.

A4. Cooling model error and effect of the grid deformation

A4.1 Evaluation of the error

The precision of a numerical model depends on the spatial and temporal step used. Here, Eq. A6 imposes that each time step depends on a space step and the stability coefficient. The space step itself depends on the number of elements chosen. Thus, the two variables controlling the accuracy of the numerical method are the number of elements (space accuracy) and the stability coefficient (time accuracy). We tested the accuracy of the cooling model by considering a uniform medium, with a constant conductivity, heat capacity and density, and neglecting the thermal contraction of elements. An initial temperature distribution inside the medium is set with a sinusoidal function, which has an analytical solution: $U(x,t) = sin(\pi x)e^{-(k/\rho C_p)t}$. The model error is estimated by computing the average temperature difference between the numerical and analytical solutions after one iteration. Figure A1 shows that the absolute average error decreases with the stability coefficient and with an increase in the number of elements. The slope of the two curves illustrates that the method is accurate to the second order in space (Fig. A1A) and the first order in time (Fig. A1B). We found that for our case the numerical solution is always hotter than the analytical one.

A4.2 Effect of the grid deformation

All previous studies using numerical modeling of lava flow thermo-elastic contractions neglected the potential effects of grid deformation on heat diffusion and in turn to the estimated displacements (Wittmann et al., 2017). This was either a choice made by the authors or was imposed by the numerical method employed. The advantage of using FEM, is that it takes into account the thermally induced grid deformations on the heat diffusion because the grid points are allowed to move. In order to quantify the actual effect of grid deformation, we performed two simulations with the same initial condition and input parameters. The first simulation takes the grid deformation into account in the cooling model, whereas the second one ignores it. Figure A2 displays the evolution of the differences between the two simulations on the vertical subsidence rate. It shows that the deformation rate difference is not constant with time. It starts to increase at the beginning of the simulation and reaches a maximum of ~3.5% after 1 month. This difference then decreases and tends to stabilize after about ten months to a value ~2.6%. It should be noted that if grid deformation is not taken into account, then the deformation rate is always underestimated. Our results indicate that ignoring grid deformation seems a reasonable assumption for characterizing lava flow behavior given the uncertainties of the thermal properties.

Supplementary references:

Deville, M.O., Fischer, P.F., Mund, E.H., 2002. High-order methods for incompressible fluid flow. Cambridge university press.

Recktenwald, G.W., 2004. Finite-difference approximations to the heat equation. Mech. Eng. 10, 1–27.

Zienkiewicz, O.C., Taylor, R.L., Taylor, R.L., 2000. The finite element method: solid mechanics. Butterworth-heinemann.

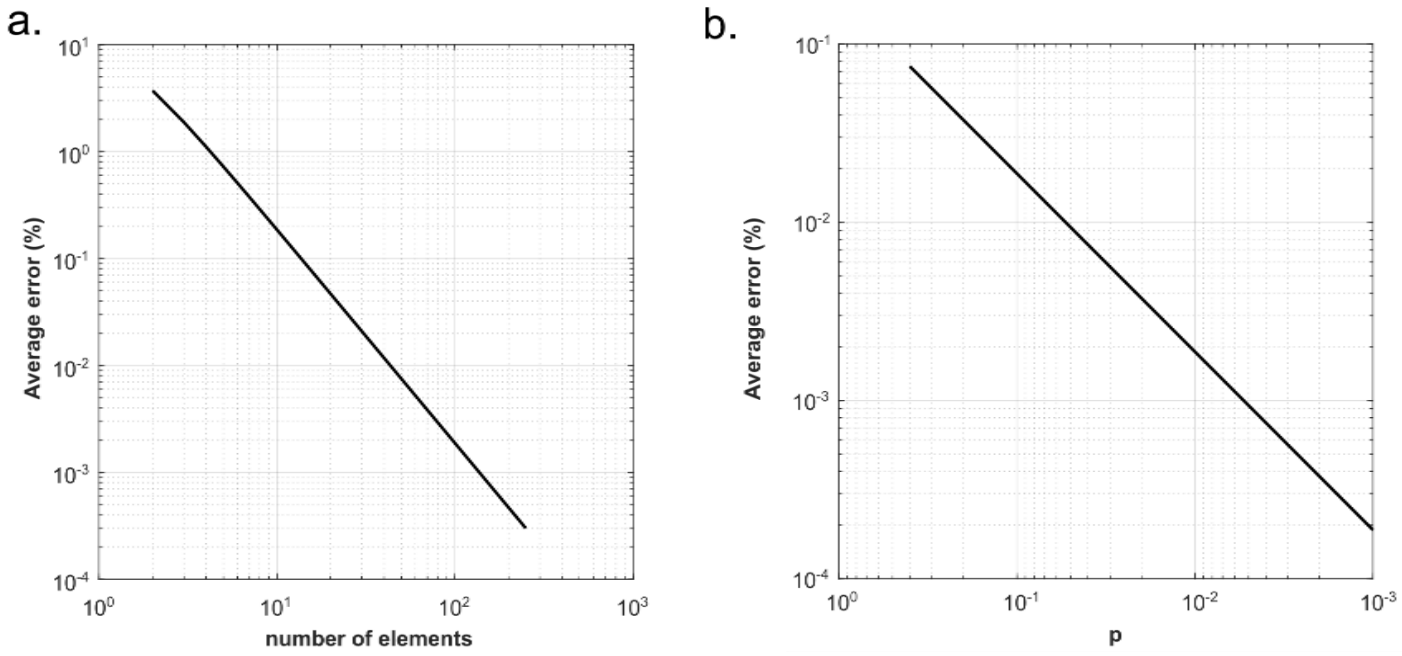

Figure A1 : Estimation of the cooling model error. **[A]** Error in space after 1 time step, function of number of elements used. The error is taken as the average temperature difference (in percent) between the numerical and analytical solutions at the grid nodes with a coefficient p=0.01. **[B]** Error in time after 1 time step, function of the coefficient p, with 100 elements.

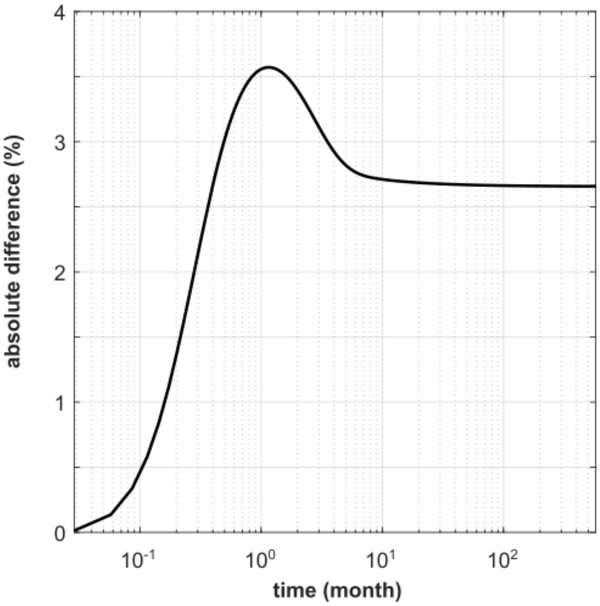

Figure A.2 : Absolute difference percentage obtained on the vertical deformation rate when comparing numerical result without grid deformation, with the result obtained taking into account the grid deformation. The time axis has a logarithmic scale in order to highlight the difference evolution during the first months of the simulation.